Low-order modeling of collective dynamics of four ring-coupled turbulent thermoacoustic oscillators

Yu Liao · Yu Guan [ID] **· Peijin Liu · Kihun Moon · Kyu Tae Kim**

Abstract We investigate the low-order modeling of collective dynamics in a can-annular combustor consisting of four ring-coupled turbulent lean-premixed combustors. Each combustor is treated as an individual thermoacoustic oscillator, and the entire combustion system is modeled using four Van der Pol oscillators ring-coupled with dissipative, time-delay, and reactive coupling terms. We show that this model, despite its simplicity, can reproduce many collective dynamics observed in experiments under various combinations of equivalence ratios and combustor lengths, such as 2-can anti-phase synchronization, alternating anti-phase synchronization, pairwise anti-phase synchronization, spinning azimuthal mode, and 4 steady thermoacoustic oscillators. The phase relationship in the majority of cases can be quantitatively modeled. Moreover, by incorporating a reactive coupling term, the model is able to reproduce the frequency shift observed experimentally. This study demonstrates the feasibility of using a simple low-order model to reproduce collective dynamics in complex turbulent combustion systems. This suggests that this model could be used (i) to facilitate the interpretation of experimental data within the synchronization framework, (ii) to identify potential parameter regimes leading to amplitude death, and (iii) to serve as a basis for modeling the collective dynamics observed in more complicated multi-combustors.

Y. Liao · Y. Guan (✉)
Department of Aeronautical and Aviation Engineering, The Hong Kong Polytechnic University, Hung Hom, Hong Kong, China
e-mail: yuguan@polyu.edu.hk

Y. Liao · P. Liu
Solid Rocket Propulsion National Laboratory, Northwestern Polytechnical University, Xi'an 710072, China

K. Moon · K. T. Kim
Department of Aerospace Engineering, Korea Advanced Institute of Science and Technology, Daejeon 34141, Republic of Korea

K. Moon
CAPS Laboratory, Department of Mechanical and Process Engineering, ETH Zürich, 8092 Zurich, Switzerland

1 Introduction

Thermoacoustic instability has posed a persistent challenge in combustion systems for decades [1,2], which often arises when the phase difference between pressure oscillation and the heat release rate fluctuation lies within a range of $\pm\pi/2$ according to the Rayleigh criterion [3]. Strong pressure oscillations generated by thermoacoustic instability can cause deviations from normal operating conditions and severe structural damage to the combustion systems [4–6].

Can-annular combustors, widely used in heavy-duty gas turbines, consist of multiple individual tubular combustors interconnected through an annulus between the combustor outlet and the turbine inlet [7]. The presence of the annulus introduces acoustic communication

between adjacent combustors, resulting in more complex dynamical characteristics of thermoacoustic instability in multi-combustor (can-annular) systems than single combustor systems [8]. To gain a deeper understanding of the modal pattern and underlying physical mechanisms associated with acoustic communication, researchers recently have undertaken experimental and numerical studies in can-annular combustors. Moon et al. [9,10] experimentally identified multiple modal patterns in a can-annular combustor consisting of four turbulent lean-premixed combustors, including push-push modes, 2-can/alternating/pairwise push-pull modes, and spinning azimuthal modes under various symmetric/asymmetric combinations of equivalence ratios and combustor lengths. Guan et al. *al*. [11] demonstrated that modifying the swirler configuration to alter the flame response distribution can change the modal pattern in the same can-annular combustor, suggesting the potential for passive control of thermoacoustic instability by manipulating the flame response distribution. The choice of fuel also significantly affects the modal pattern in can-annular combustors. Moon et al. [12] observed higher frequencies of thermoacoustic modes when burning pure hydrogen in a can-annular combustor compared to methane [9,10], and discovered new modal patterns such as localized push-push and localized push-pull modes. The acoustic communication between adjacent combustors through the cross-talk section also plays a crucial role in determining the modal patterns. Buschmann et al. *al*. [13] experimentally investigated the effect of asymmetric acoustic communication between adjacent combustors on the thermoacoustic instability in a can-annular combustor consisting of eight combustors. They found that the modal pattern, as well as the frequency and amplitude of pressure oscillation were strongly influenced by modifying the dimensions and configurations of the coupling element between cans. However, the mode localization, which is a phenomenon previously observed in can-annular combustors due to the presence of asymmetries of the system (e.g., the flame response [14]) is not observed. In terms of numerical studies, Ghirardo et al. first revealed the presence of clustered unstable thermoacoustic modes with closely spaced frequencies, and attributed mode localization to symmetry-breaking configurations in the can-annular combustors [14,15]. von Saldern et al. [16] later provided an analytical explanation to the clustered unstable thermoacoustic modes using a low-order

network model with Bloch boundary conditions, which was subsequently examined in experiments by Humbert et al. [17]. von Saldern et al. [18] also investigated the influence of the number of cans on thermoacoustic instability in can-annular combustors, and found that as the number of cans decreases (to four cans), quasiperiodic oscillation with three equally spaced frequencies can emerge. Haeringer et al. [19,20] proposed a hybrid low-order modeling approach, which combined the computational fluid dynamics simulation of the burner/flame zone with Bloch boundary conditions, enabling the time-domain simulation of thermoacoustic instability in can-annular combustors with low computational cost. Additionally, Fournier et al. [21] explored the interaction between clusters of acoustic and intrinsic thermoacoustic modes in can-annular combustors.

In recent years, a novel approach based on synchronization theory has been developed by researchers to study thermoacoustic instability [22,23]. This approach treats each combustor experiencing thermoacoustic instability as an individual self-excited thermoacoustic oscillator, enabling the application of synchronization theory to interpret and model the phase and amplitude dynamics in both laminar and turbulent multi-combustor systems. For example, Hyodo et al. [24] experimentally examined how changing the dimensions and number of coupling tubes can affect the emergence of amplitude death in two coupled Rijke tubes powered by laminar premixed flames. Amplitude death refers to the global suppression of oscillation when multiple oscillators are coupled in a specific manner [25] and can be potentially utilized for designing passive control systems for thermoacoustic instability. On the turbulent front, using concepts from mutual synchronization, Jegal et al. [26] reported various collective dynamics, including phase locking, two-frequency quasiperiodicity, and amplitude death in two turbulent lean-premixed combustors coupled through a crosstalk tube. Moon et al. [27] later examined the influence of geometric dimensions of the cross-talk tube on collective dynamics as well as the dissipative and time-delay coupling between the two thermoacoustic oscillators in the same experimental system. Guan et al. [28] extended this approach to study thermoacoustic instability in a can-annular combustor consisting of four cans. They proposed a hybrid approach combining complex systems methods and unsupervised machine learning techniques to investigate both the

flame-acoustic interaction occurring within an individual can and the acoustic-acoustic interactions occurring between adjacent cans, and showed that the latter type of interaction played a more crucial role in determining the collective dynamics. It is also worth noting that fruitful results have been obtained in coupled thermoacoustic systems without combustion using such an approach [29–32].

Although the studies discussed above provide valuable insights into the interactions between thermoacoustic modes, modeling such interactions would offer a more practical means for the prediction and control of such collective dynamics. Different from the typical low-order/reduced-order network modeling approach for can-annular combustors [14,16,33–36], where significant efforts were dedicated to appropriately describing the physics of acoustic communication between cans, the low-order modeling approach we adopt in this study focuses on reproducing dynamics observed in experiments with minimal computational cost. In this approach, the model is constructed using simple low-order oscillators (e.g., Van der Pol (VDP) oscillator) coupled with coupling, time-delay, and forcing terms. This latter approach has been recently used to model the bifurcation dodge by ramping the air flow rate in a turbulent combustor [37], the mutual synchronization of thermoacoustic modes in a sequential combustor [38], the slanted mode in an annular combustor [39], the intermittency in a single turbulent combustor [40], the mutual synchronization between two coupled turbulent lean-premixed combustors [41], the transition to thermoacoustic instability in both laminar and turbulent combustors [42,43], the intermittent energy transfer between Bloch waves in a can-annular combustor [44], and nonlinear dynamics of pure intrinsic thermoacoustic modes [45]. Building upon our previous modeling work [41], where we use two dissipative and time-delay coupled VDP oscillators to reproduce several collective dynamics experimentally observed in Refs. [26,27], in this study, we apply this model to a can-annular combustion system consisting of four ring-coupled combustors and reproduce more complex collective dynamics experimentally reported in Ref. [9,10]. This work further examines the feasibility of reproducing collective dynamics using low-computational-cost, simply-structured low-order models in a complex combustion system.

2 Experimental set-up and low-order model

We provide a brief overview of the experimental setup used in Refs. [9,10]. As shown in Fig. 1a–c, the experimental setup consists of four identical turbulent lean-premixed combustors. These combustors are interconnected by four identical cross-talk tubes (length: $l_{XT} = 400$ mm and inner diameter: $D_{XT} = 43$ mm) in a ring configuration, which form an annular cross-talk section. The combustor length, ξ_{XT}, can be adjusted by changing the position of the cross-talk section and a movable piston. In this study, we investigated three different values of ξ_{XT} (1000/1300/1600 mm). Following our previous study [27], we expressed them in three values of a dimensionless number η (0.40, 0.31, 0.25), which is defined as l_{XT}/ξ_{XT}. We consider four equivalence ratios of CH$_4$/air, namely $(\phi_a, \phi_b, \phi_c, \phi_d)$=(0.57, 0.61, 0.65, 0.69). Given a η, we consider three types of equivalence ratio combinations for four combustors $(\phi_1, \phi_2, \phi_3, \phi_4)$: (a) uniform equivalence ratios, i.e., $(\phi_1 = \phi_2 = \phi_3 = \phi_4)$, (b) alternating equivalence ratios, i.e., $(\phi_1 = \phi_3, \phi_2 = \phi_4)$, and (c) pairwise equivalence ratios, i.e., $(\phi_1 = \phi_2, \phi_3 = \phi_4)$. This is achieved by adjusting the mass flow rate of CH$_4$ and air for each combustor separately using mass flow controllers (Teledyne Instruments model HFM-D-301 for CH$_4$, and Sierra Instruments model FlatTrak 780 S for air). For all experiments, we keep the bulk velocity and the inlet temperature of the fuel-air mixture at constant values of $\bar{u}_i = 20.0$ m/s and $T_{inlet,i} = 200$ °C, respectively. The Reynolds number for this inlet condition is approximately 22,000 and remains constant across all cases. We measure the pressure oscillations in each combustor using piezoelectric transducers (PCB model 112A22: sensitivity 14.5 mV/kPa, uncertainty $\pm 1.0\%$) mounted at the injector plane (indicated by p' in Fig. 1b). We chose the pressure signal measured at this measurement location for having a reliable signal-to-noise ratio shown by Moon et al. [9]. We sample the pressure signals at a rate of 12 kHz on a data acquisition system (TEAC model LX-110). For further comprehensive information on the experimental setup and operating conditions, please refer to the relevant literature [9,10].

Next, we proceed to introduce our low-order modeling approach. We first consider the four ring-coupled combustors in the can-annular combustion system as
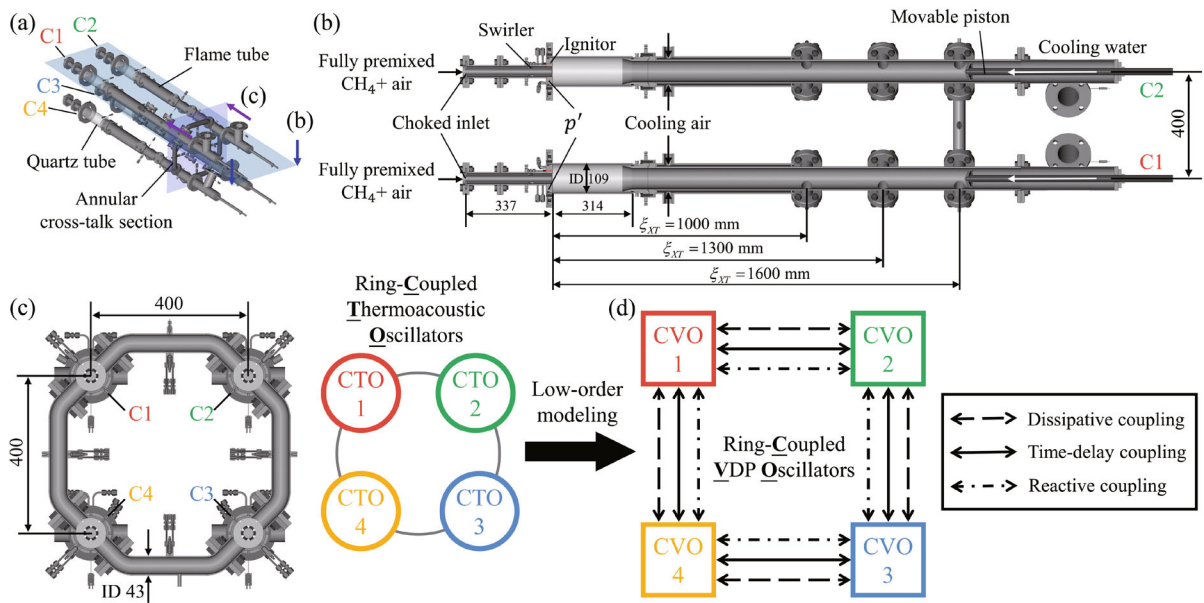
Fig. 1 Experimental setup consisting of four turbulent thermoacoustic oscillators ring-coupled through a cross-talk section: **a** isometric view, **b** cross-sectional view of two adjacent combustors, **c** cross-sectional view of the cross-talk section (left) and the network structure of ring-coupled thermoacoustic oscillators (CTO1 to CTO4 in clockwise order). The dimensions are in mil-

limeters. More details about this setup can be found in Refs. [9,10]. Panel **d** shows the ring-coupled VDP oscillators (CVO1 to CVO4 in clockwise order). They are coupled with dissipative coupling (dashed line), time-delay coupling (solid line), and reactive coupling (dash-dotted line)

four coupled thermoacoustic oscillators (CTOs) in a ring configuration. For each individual decoupled thermoacoustic oscillator (DTO), its dynamical properties are determined by its operating conditions (different η and ϕ). Each DTO can exhibit one of two distinct states: a fixed point and a limit cycle. We adopt the low-order modeling framework used in our previous study [41] and use four coupled Van der Pol oscillators (CVOs) in a ring configuration to model the corresponding four CTOs. Despite subtle differences in the equation of low-order models, these low-order canonical models, which have been widely used in previous studies to qualitatively model dynamical behavior of thermoacoustic systems [30,38–41,46–49] mostly share a Van der Pol kernel, which justifies our modeling choosing. For each individual decoupled Van der Pol oscillator (DVO), its dynamical properties are determined by the oscillator parameters (λ and ω), which can also exhibit either a fixed point or a limit cycle. Four CVOs are coupled using the time-delay coupling term, dissipative coupling term, and reactive coupling term based on the following reasons: (1) The dissipative coupling and

time-delay coupling term were used to model the acoustic communication introduced by coupling two thermoacoustic oscillators before [24,29,41,50], where the coupling strength was used to quantitatively model the degree of mutual interaction between coupled thermoacoustic oscillators and the time delay was used to model the time used by acoustic waves to propagate from one thermoacoustic oscillator to affect another; (2) The reactive coupling term was incorporated because of absence of amplitude death as well as accounting for coupling-induced frequency shifts in experiments. In this study, we only include one time-delay coupling term because (1) the number of time-delay coupling terms in the low-order model is mainly associated with the number of coupling tubes in the setup in previous studies [24,30,31,41] and (2) our thermoacoustic oscillator oscillates at a single frequency, which leads to a single time scale. The structural representation of this ring-coupled oscillator model is illustrated in Fig. 1(d), and the model is defined as:

$$\ddot{x}_i - \left(\lambda_i - x_i^2\right)\dot{x}_i + \omega_i^2 x_i = \underbrace{k_d\left(\dot{x}_{i+1} + \dot{x}_{i-1} - 2\dot{x}_i\right)}_{Dissipative\ coupling}$$

$$+ \underbrace{k_\tau[\dot{x}_{i+1}(t-\tau) + \dot{x}_{i-1}(t-\tau) - 2\dot{x}_i]}_{Time-delay\ coupling}$$

$$+ \underbrace{k_r\left(x_{i+1} + x_{i-1} - 2x_i\right)}_{Reactive\ coupling} \quad (1)$$

where the subscripts $i = 1, 2, 3, 4$ represent the CVO1 to CVO4, and the subscript $i + 1$ and $i - 1$ in Eq. (1) refer to the oscillators adjacent to oscillator i. For example, for the CVO4 that represents CTO4, its adjacent CVOs are CVO1 and CVO3, which represent CTO1 and CTO3, respectively. For each VDP oscillator, x_i is the dynamic variable, ω_i is the natural angular frequency, λ_i is the excitation and damping parameter that control whether the VDP oscillator evolves to a fixed point ($\lambda_i < 0$) or to a limit cycle ($\lambda_i > 0$) [51]. The RHS of Eq. (1) are the coupling terms. k_d, k_τ, k_r, and τ are the dissipative coupling strength, the time-delay coupling strength, the reactive coupling strength, and the time delay, respectively.

We calibrate the model using the experimental data from Refs. [9,10]. To facilitate this, given a η, we first normalize the pressure amplitude of DTOs with respect to the maximum pressure amplitude of all DTOs, i.e., $\tilde{p}' = p'/p'_{max}$, and then normalize the frequency with respect to the frequency of p'_{max}, i.e., $\tilde{f} = f/f_{p'_{max}}$. Subsequently, we separately tune λ_i and ω_i of DVOs to match $\tilde{p}$ and $\tilde{f}$ of DTOs. $\beta_i = (\lambda_i, \omega_i)$ is used to represent each group of oscillator parameters λ_i and ω_i. The disparity between the normalized values obtained from experiments and simulations is less than 3.0% and 0.5%, respectively, which is negligible considering the simplicity of the model. Besides, we neglect the influence of asymmetries caused by uncertainties in the combustors on the properties of nominally identical CTOs. This means that we assign the same values of λ_i and ω_i to CVOs representing CTOs that share the same ϕ. Consequently, the pressure and frequency ratios obtained through simulations may not closely resemble those observed in experiments. Although finely tuning λ_i and ω_i for CVOs can mitigate this discrepancy (see Appendix A), we choose not to adopt this approach because we would like to maintain the simplicity of the equation and its parameters calibration in this study. As for calibrating the coupling parameters (k_d, k_τ, k_r, and τ) for CVOs, we take the following procedures. For k_d

and k_τ, we adopt the same assumption made in [41] when low-order modeling two CTOs, namely $k_d = k_\tau$. This is because we believe that the time-delay and dissipative effects induced by the cross-talk section for two adjacent combustors in this ring-coupled combustion system are qualitatively similar to those induced by the connecting tube between two combustors in [41]. Additionally, we assume that both k_d and k_τ decrease as ξ_{XT} increases. This is due to the fact that acoustic waves require more time to travel from one combustor's flame to another as ξ_{XT} increases (i.e. a smaller η). Ideally, the two flames will have minimal interaction if ξ_{XT} is sufficiently long. Consequently, this implies a smaller k_d and k_τ (weaker coupling between two oscillators) as ξ_{XT} increases. A similar relationship holds true for the time delay τ but in an opposite way (i.e. τ increases if ξ_{XT} increases). What is different from the previous model [41] is the incorporation of a reactive coupling term in Eq. (1) to primarily address the frequency shift seen in the spectra of CTOs. Reactive coupling refers to a type of coupling that does not involve energy loss (damping) during the energy transformation [52,53]. In contrast to dissipative coupling, which positions the synchronous frequency of detuning oscillators between their natural frequencies, reactive coupling often leads to a higher synchronous frequency than the two natural frequencies [51]. Moreover, when reactive coupling dominates over dissipative and time-delay coupling, amplitude death rarely occurs [54]. Our experiments under various operating conditions did not reveal any instances of amplitude death [9,10], further supporting the inclusion of reactive coupling term in the model. When tuning k_d, k_τ, k_r, and τ, our focus lies in qualitatively reproducing the collective dynamics observed in experiments [9,10], rather than achieving precise quantitative replication of pressure amplitude and frequency ratios. This approach stems from our intention to model the collective dynamics of the experimental system, rather than striving for an exact reproduction of the intricate characteristics of the experimental flow field. The latter task is better suited for high-fidelity computational fluid dynamics tools, which entail higher computational costs compared to our low-order modeling approach. The sensitivity analysis for turbulent combustion noise (refer to Appendix B) and the parametric noise for all calibrated parameters (refer to Appendix C) have been conducted separately. We use the 4th order Runge–Kutta method to solve the Eq. (1) numerically.
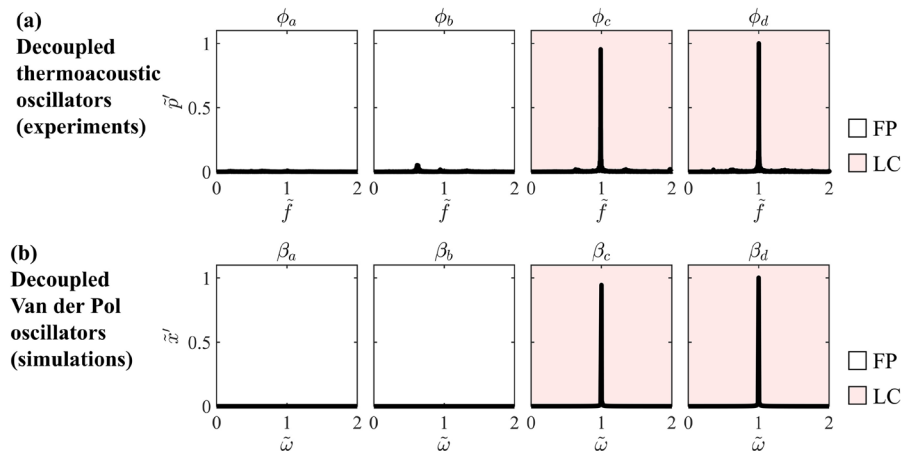
Fig. 2 Spectral comparison between **a** decoupled thermoacoustic oscillators when $\eta_1 = 0.40$ (experiments) and **b** decoupled VDP oscillators (simulations). Each β_i ($i = a, b, c, d$) denotes a combination of λ_i and ω_i in simulations as per $(\phi_a, \phi_b, \phi_c, \phi_d) = (0.57, 0.61, 0.65, 0.69)$ in experiments. $\beta_i = $ (λ_i, ω_i) of each decoupled VDP oscillator is calibrated using $\tilde{p}'$ and $\tilde{f}$ of its corresponding thermoacoustic oscillator, which gives $\beta_a = (\lambda_a, \omega_a) = (-0.01, 0.97)$, $\beta_b = (\lambda_b, \omega_b) = (-0.01, 0.98)$, $\beta_c = (\lambda_c, \omega_c) = (0.042, 1)$, $\beta_d = (\lambda_d, \omega_d) = (0.05, 1)$. Legend: FP = fixed point; LC = limit cycle

3 Results and discussion

Given a chosen $\eta = 0.40/0.31/0.25$, three types of ϕ combinations were examined: uniform, alternating and pairwise, and four values of ϕ were tested as per $(a, b, c, d) = (0.57, 0.61, 0.65, 0.69)$ in Refs. [9,10]. In this study, we select the representative cases in experiments to compare them against the simulations as some cases exhibit similar collective dynamics. For each η_i, we first show the spectral comparison between DTOs (experiments) and DVOs (simulations). We then show the spectral comparison between CTOs (experiments) and CVOs (simulations). We last show the phase relationship comparison between CTOs and CVOs. To calculate the specific phase of each oscillator, for the cases showing only one peak, we apply a bandpass filter around that peak with a bandwidth of 2 Hz. For the cases showing multiple peaks (e.g., Fig. 3(E3) and Fig. 9(E1)), we apply a bandpass filter around the chosen peak with a bandwidth of 2 Hz. After applying the bandpass filter, we proceed to use the Hilbert transform to obtain the instantaneous phase of each signal and calculate the instantaneous phase difference between ith CTO/CVO and the 1st CTO/CVO, i.e., $\psi_{\tilde{p}',i} = \varphi_{\tilde{p}',i} - \varphi_{\tilde{p}',1}$ or $\psi_{\tilde{x}',i} = \varphi_{\tilde{x}',i} - \varphi_{\tilde{x}',1}$.

3.1 Short combustor: $\eta_1 = 0.40$

We start by examining the spectral comparison between DTOs (experiments) and DVOs (simulations) for $\eta_1 = 0.40$ in Fig. 2. The state of each case is differentiated using the background color (white: fixed point; light pink: limit-cycle). The DTO is a fixed point when $\phi \leqslant 0.61$, and a limit cycle when $\phi \geqslant 0.65$ in Fig. 2a. The DVO behaves similarly in terms of β change in Fig. 2b.

We now proceed to examine the spectral and phase relationship comparison between CTOs (experiments) and CVOs (simulations) for $\eta_1 = 0.40$ in Figs. 3 and 4. To facilitate the spectral comparison, we use a waterfall-like plot to show four CTOs/CVOs, 1–4, along x-axis, normalized frequency, $\tilde{f}$ or $\tilde{\omega}$, along y-axis, and spectral amplitude, $\tilde{p}'$ or $\tilde{x}'$, along z-axis. Two distinct collective dynamics observed in experiments can be reproduced in simulations: 2-can Anti-phase Synchronization (2AS, green background in Figs. 3 and 4) and 4 Steady Thermoacoustic Oscillators (4STO, gray background in Figs. 3 and 4). In the case of 2AS, only two opposite CTOs are self-excited and anti-phase synchronized (their phase difference $|\psi_{i,j}| > \pi/2$), while the remaining two opposite CTOs are steady. This dynamical state corresponds to a first-order standing
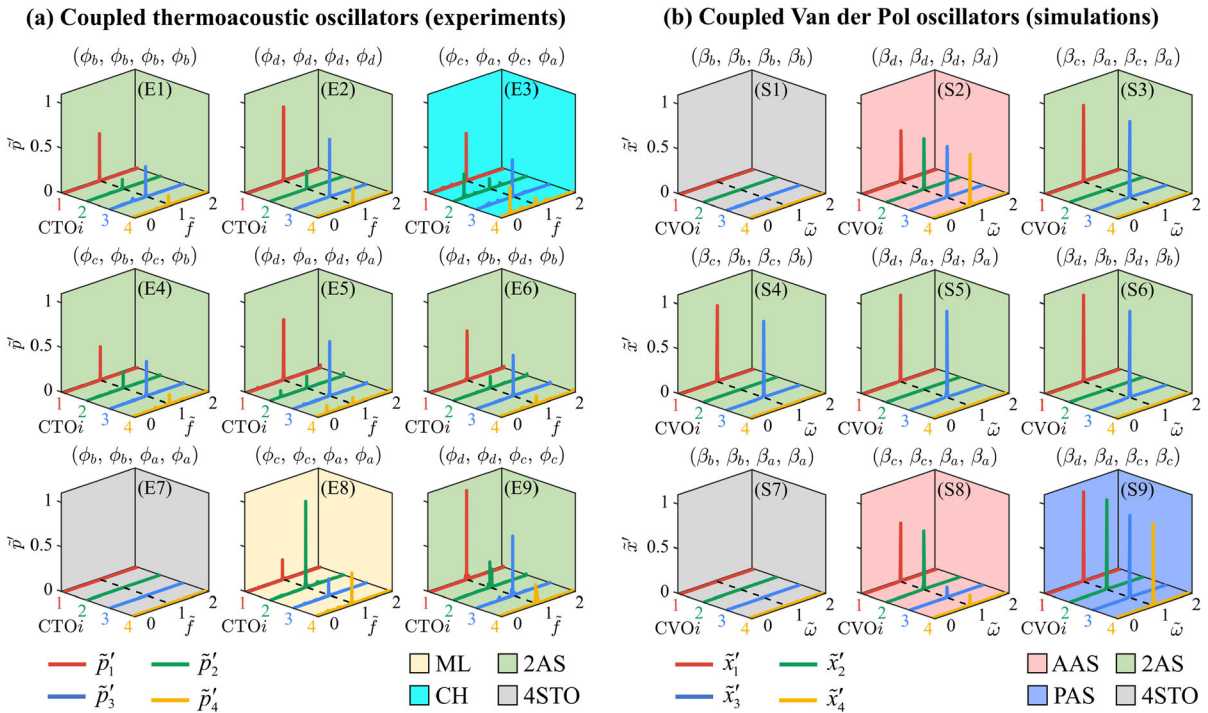
Fig. 3 Spectral comparison between **a** coupled thermoacoustic oscillators when $\eta_1 = 0.40$ (experiments) and **b** coupled VDP oscillators (simulations). ϕ_i of each thermoacoustic oscillator and β_i of each VDP oscillator are shown at the top of each subfigure in an order from thermoacoustic/VDP oscillator 1 to 4. β_i of the coupled case is kept the same with its corresponding decoupled case. Coupling parameters (k_d, k_τ, k_r, τ) of the cou-

pled VDP oscillators are calibrated using experimental results, which gives $k_d = k_\tau = 0.005$, $k_r = 0.005$, and $\tau = 1$. The dashed line in the subfigure denotes the position of $\tilde{f} = 1$ and $\tilde{\omega} = 1$, respectively. Legend: 2AS = 2-can anti-phase synchronization; AAS = alternating anti-phase synchronization; PAS = pairwise anti-phase synchronization; 4STO = 4 steady thermoacoustic oscillators; ML = mode localization; CH = weak chimera

azimuthal mode whose nodal line lies in the two opposite stable combustors, which is also known as a 2-can push-pull mode [9,10]. For example, Fig. 3(E5) shows that peaks of $\tilde{p}'_1$ (red) and $\tilde{p}'_3$ (blue) are prominent whereas those of $\tilde{p}'_2$ (green) and $\tilde{p}'_4$ (yellow) remain negligible. Meanwhile, Fig. 4(E5) shows $\psi_{\tilde{p}',3}$ remains constant with a mean value lying within the range of $|\psi| > \pi/2$, indicating anti-phase synchronization between the two thermoacoustic oscillators. These two features are reproduced numerically by the model in Fig. 3(S5) and Fig. 4(S5). In the case of 4STO, where four steady DTOs are ring-coupled, the corresponding CTOs remain steady. For example, Fig. 3(E7) shows that peaks of CTOs remain negligible. Figure 4(E7) therefore shows no curve. These two features are also reproduced numerically by the model in Fig. 3(S7) and Fig. 4(S7). However, we notice that some of the collec-

tive dynamics observed in experiments cannot be reproduced in simulations. When four steady DTOs are ring-coupled, a coupling-induced unstable thermoacoustic mode can emerge only in two opposite combustors (i.e. 2AS) as shown in Fig. 3(E1). But the model still numerically produces 4STO in Fig. 3(S1). When four DTOs ring-coupled under the pairwise ϕ combination with two of them being steady and the remaining two being unsteady, mode localization (ML, Fig. 3(E8)) can emerge, but only in the short combustor. ML, which was often seen in weakly coupled systems [55], was previously attributed to asymmetry in the coupled thermoacoustic system, such as asymmetric flame response [14]. When ML emerges, the thermoacoustic mode is locally "trapped" in a specific combustor. As shown in Fig. 3(E8), the localized thermoacoustic mode exhibits a significantly larger amplitude in CTO2 (green line)
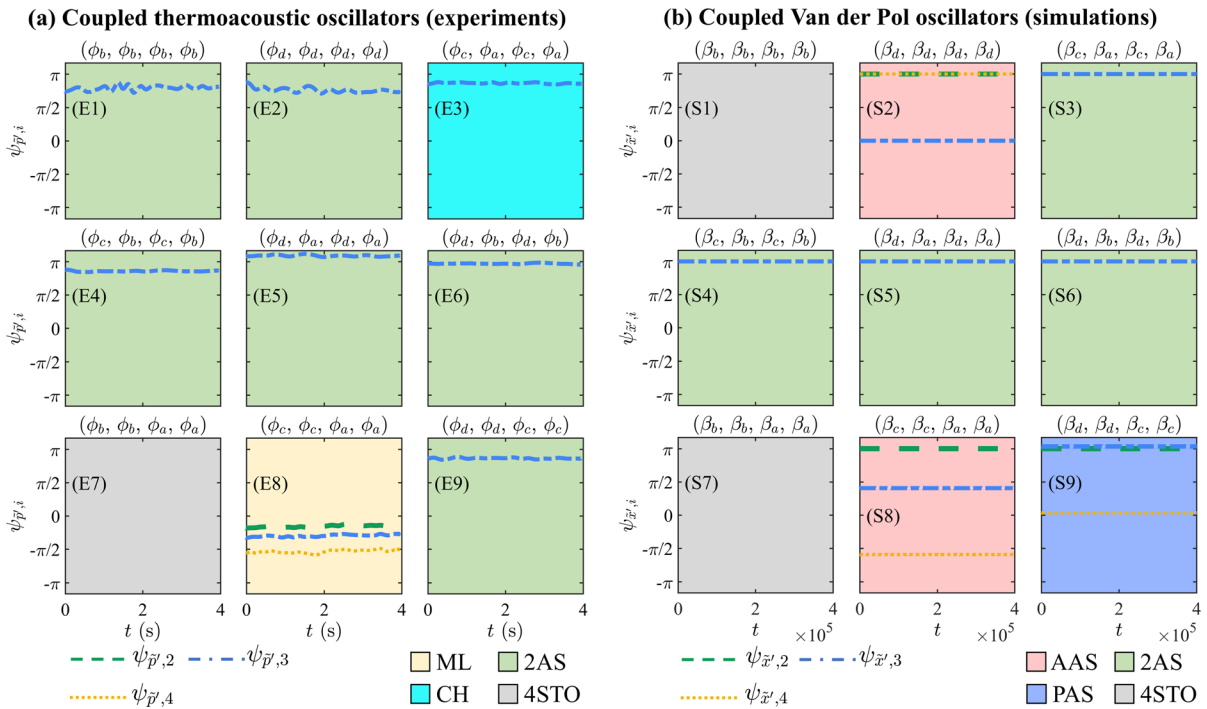
Fig. 4 Phase relationship comparison between **a** coupled thermoacoustic oscillators when $\eta_1 = 0.40$ (experiments) and **b** coupled VDP oscillators (simulations). $\psi_{\tilde{p}',i}$ and $\psi_{\tilde{x}',i}$ denotes the instantaneous phase difference between ith coupled thermoacoustic oscillator/coupled VDP oscillator and the 1st coupled thermoacoustic oscillator/coupled VDP oscillator. For the case of 2AS, we show only one curve of the instantaneous phase difference because there are only 2 self-excited oscillators. For the case of 4STO, we show no curve of the instantaneous phase difference because there is not any self-excited oscillator. For other cases, we show three curves of the instantaneous phase difference. Legend: 2AS = 2-can anti-phase synchronization; AAS = alternating anti-phase synchronization; PAS = pairwise anti-phase synchronization; 4STO = 4 steady thermoacoustic oscillators; ML = mode localization; CH = weak chimera

than the other three oscillators. Although the spectrum numerically produced by the model appears to be similar to that in experiments (Fig. 3(S8) → (E8)), the phase relationship is missing. In the case of ML (Fig. 4(E8)), CTO2 and CTO3 are in-phase synchronized with CTO1 ($|\psi_{\tilde{p}',2}| < \pi/2$ and $|\psi_{\tilde{p}',3}| < \pi/2$), while CTO4 is anti-phase synchronized with CTO1 ($|\psi_{\tilde{p}',4}| > \pi/2$). However, in its corresponding numerical case, only CVO3 is in-phase synchronized with CVO1, while CVO2 and CVO4 are anti-phase synchronized with CVO1 (Fig. 4(S8)). When four DTOs under the alternating ϕ combination with two of them being steady and the remaining two being unsteady, a weak anti-phase chimera (Fig. 3(E3)) can emerge. This state involves two groups of internally synchronized oscillators with different synchronous frequencies, while inter-group synchronization is desynchronized, which was initially defined by Ashwin et al. [56]. The presence of such a state was reported both experimentally and numerically in various systems [57–59]. The model fails numerically reproducing this phenomenon because it is unable to produce the second nonlinear unstable mode which is excited after two steady DVOs are coupled with two unsteady DVOs (Fig. 3(S3) → (E3)). Nonetheless, we focus only on the dominant mode near $\tilde{f} = 1$, the anti-phase relationship between CTO1 and CTO3 is captured numerically by the model with $|\psi_{\tilde{p}',3}| > \pi/2$ (Fig. 4(S3) → (E3)).

3.2 Medium combustor: $\eta_2 = 0.31$

Next, we consider the collective dynamics for $\eta_2 = 0.31$. We start by examining the spectral comparison between DTOs (experiments) and DVOs (simulations). The dynamical behavior of DTOs under differ-
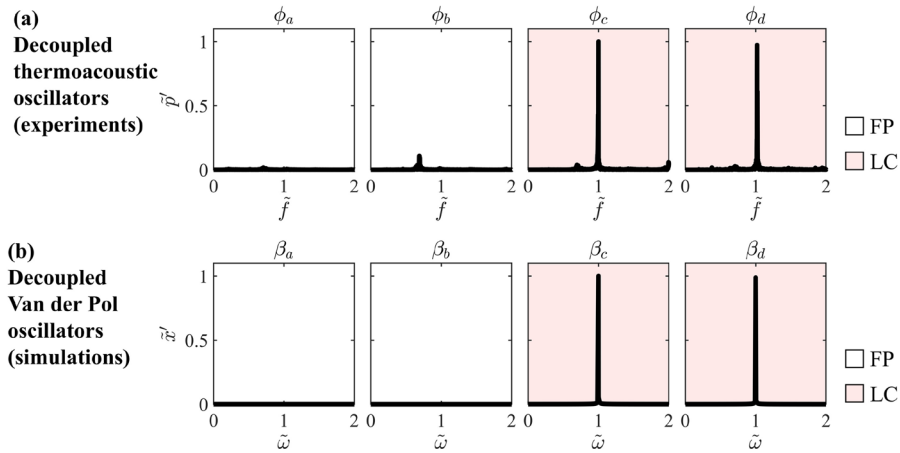
Fig. 5 The same as for Fig. 2 but when $\eta_2 = 0.31$. Each β_i ($i = a, b, c, d$) denotes a combination of λ_i and ω_i in simulations as per $(\phi_a, \phi_b, \phi_c, \phi_d)$=(0.57, 0.61, 0.65, 0.69) in experiments. $\beta_i = (\lambda_i, \omega_i)$ of each decoupled VDP oscillator is calibrated using $\tilde{p}'$ and $\tilde{f}$ of its corresponding thermoacoustic oscillator, which gives $\beta_a = (\lambda_a, \omega_a) = (-0.02, 0.99)$, $\beta_b = (\lambda_b, \omega_b) = (-0.02, 0.99)$, $\beta_c = (\lambda_c, \omega_c) = (0.05, 1)$, $\beta_d = (\lambda_d, \omega_d) = (0.048, 1)$. Legend: FP = fixed point; LC = limit cycle
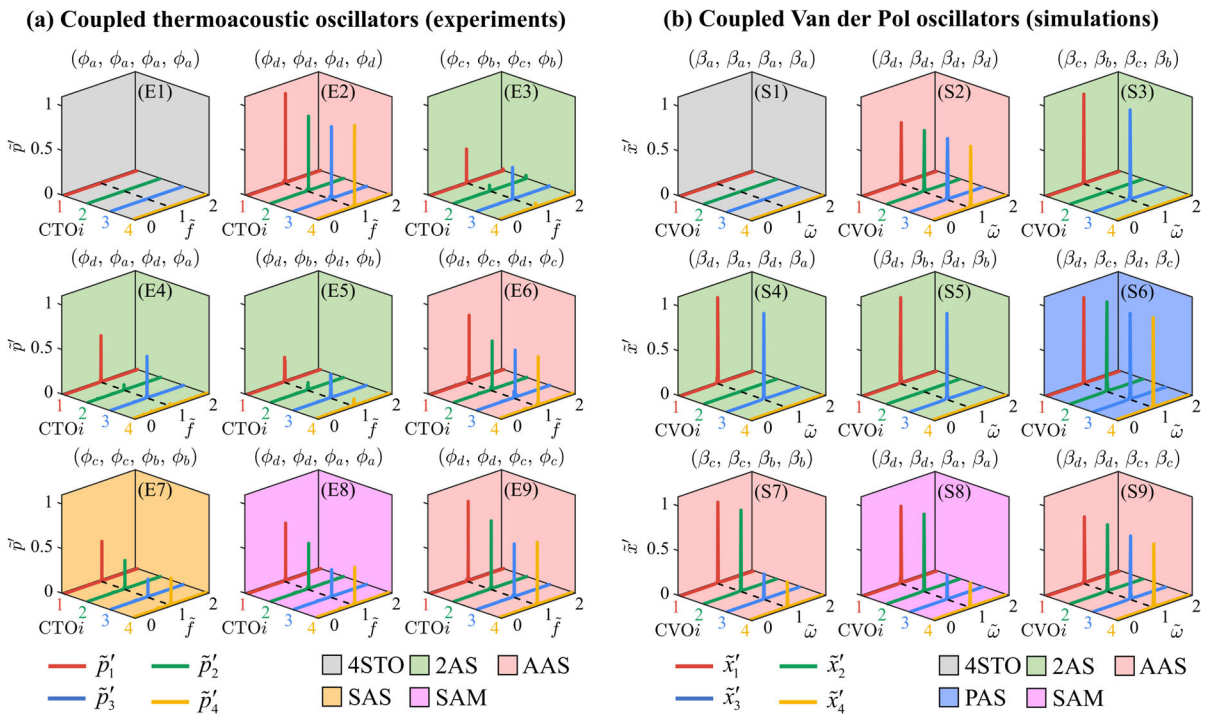
Fig. 6 The same as for Fig. 3 but when $\eta_2 = 0.31$. Coupling parameters (k_d, k_τ, k_r, τ) of the coupled VDP oscillators are calibrated using experimental results, which gives $k_d = k_\tau = 0.004$, $k_r = 0.01$, $\tau = 1.3$. Legend: 2AS = 2-can anti-phase synchronization; AAS = alternating anti-phase synchronization; PAS = pairwise anti-phase synchronization; 4STO = 4 steady thermoacoustic oscillators; SAS = superposition of anti-phase synchronization; SAM = spinning azimuthal mode
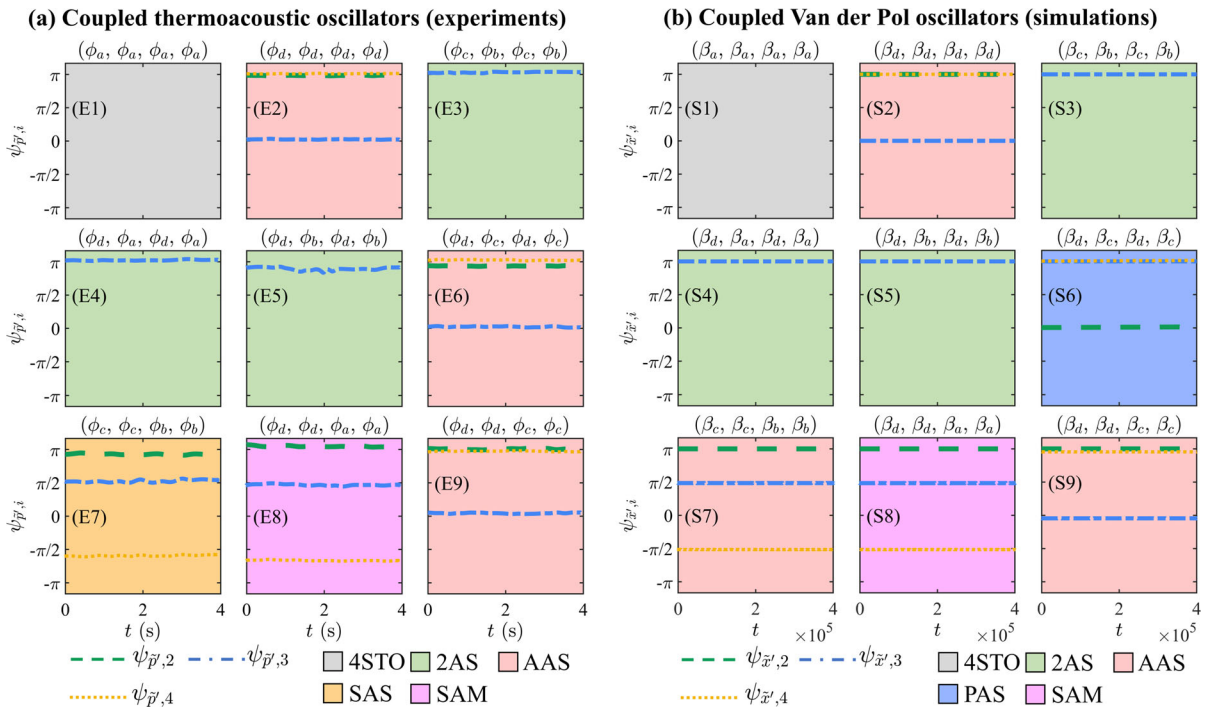
Fig. 7 The same as for Fig. 4 but when $\eta_2 = 0.31$. Legend: 2AS = 2-can anti-phase synchronization; AAS = alternating anti-phase synchronization; PAS = pairwise anti-phase synchro-

nization; 4STO = 4 steady thermoacoustic oscillators; SAS = superposition of anti-phase synchronization; SAM = spinning azimuthal mode

ent equivalence ratios is consistent with those observed for $\eta_1 = 0.40$, where two fixed points are present for $\phi \leqslant 0.61$ and two limit cycles occur for $\phi \geqslant 0.65$ in Fig. 5(a). The DVO behaves similarly in terms of β change in Fig. 5(b).

Apart from 2AS and 4STO, two new kinds of collective dynamics observed in experiments can be reproduced in simulations for $\eta_2 = 0.31$: Alternating Antiphase Synchronization (AAS, salmon background in Figs. 6 and 7) and Spinning Azimuthal Mode (SAM, magenta background in Fig. 6 and Fig. 7). In the case of AAS, each CTO is anti-phase synchronized with its two adjacent CTOs ($|\psi| > \pi/2$) and in-phase synchronized with its opposite CTO ($|\psi| < \pi/2$). This dynamical state corresponds to a second-order standing azimuthal mode whose two nodal lines lie within the cross-talk section, which is also known as a global alternating push-pull mode [9,10,14–16,18,60,61]. For example, Fig. 6(E2) shows that 4 peaks of $\tilde{p}'$ are all prominent, albeit with slight variations in their heights. Meanwhile, Fig. 7(E2) shows $\psi_{\tilde{p}',2}$ and $\psi_{\tilde{p}',4}$ remain constant with a mean value lying within the range of $|\psi| > \pi/2$,

indicating anti-phase synchronization between CTO1 and its two neighbors (CTO2 and CTO4). By contrast, $\psi_{\tilde{p}',3}$ remains constant with a mean value lying within the range of $|\psi| < \pi/2$, indicating in-phase synchronization between CTO1 and its diagonal oscillator (CTO3). These characteristic features are all reproduced numerically by the model in Fig. 6(S2) and Fig. 7(S2). In the case of SAM, CTOs share the same synchronous frequency but with a specific phase difference between each pair of adjacent CTOs. As reported by Moon et al. [10], the pressure signals measured in the cross-talk section have a fixed phase difference of $\pi/2$ between each pair of adjacent combustors. As for the pressure signals measured at the injector plate ($\tilde{p}'$), the phase difference is slightly different in Fig. 7(E8), where $\psi_{\tilde{p}',3} \approx \pi/2$, $\psi_{\tilde{p}',2} \approx \pi$, and $\psi_{\tilde{p}',4} \approx -\pi/2$ (i.e., $3\pi/2$). This peculiar spinning azimuthal mode is caused by the modal interaction of two degenerate eigenmodes in a can-annular combustion system consisting of four cans [10]. The special phase dynamics is accurately reproduced by the model in Fig. 7(S8), where $\psi_{\tilde{x}',3} \approx \pi/2$, $\psi_{\tilde{x}',2} \approx \pi$, and $\psi_{\tilde{x}',4} \approx -\pi/2$.

Although the model successfully reproduces the majority of the experimentally observed collective dynamics for $\eta_2 = 0.31$, it fails to reproduce some special collective behaviors. When four DTOs-two stable and two self-excited-are ring-coupled under the pairwise ϕ combination, a unique dynamical state emerges only in the medium combustor that is Superposition of Anti-phase Synchronization (SAS, gold background in Fig. 6(E7) and Fig. 7(E7)). Despite similarities existing in the FFT spectra and phase relationships, this dynamical state differs from SAM due to subtle difference in phase dynamics. In the case of SAM, the phase difference between each adjacent oscillator rigorously follows a linear relationship, while, in the case of SAS, the phase difference between each adjacent oscillator follows a much less linear relationship. We interpret this dynamical state, arising from the superposition of two pairs of anti-phase synchronized degenerated eigenmodes, as SAS in line with our previous study [10]. CTO1 is anti-phase synchronized with all other three CTOs in Fig. 7(E7), where $\psi_{\tilde{p}',2} \approx 0.93\pi$, $\psi_{\tilde{p}',3} \approx 0.53\pi$, and $\psi_{\tilde{p}',4} \approx -0.59\pi$. The model partially reproduces this distinctive collective dynamics that CVO1 is anti-phase synchronized with CVO2 ($\psi_{\tilde{x}',2} \approx \pi$) and CVO4 ($\psi_{\tilde{x}',4} \approx -0.52\pi$), while in-phase synchronized with CVO3 ($\psi_{\tilde{x}',3} \approx 0.49\pi$).

3.3 Long combustor: $\eta_3 = 0.25$

Last, we consider the collective dynamics for $\eta_3 = 0.25$. Similarly, we begin by comparing the spectra of DTOs (experiments) and DVOs (simulations). The dynamical behavior of DTOs under various equivalence ratios differs from those observed for $\eta_1 = 0.40$ or $\eta_2 = 0.31$, where the DTO is a limit cycle only when $\phi = 0.61$, while a fixed point for other three ϕs, as shown in Fig. 8a. The DVO behaves similarly in terms of β change in Fig. 8b.

A new kind of collective dynamics observed in experiments is reproduced in simulations for $\eta_3 = 0.25$: Pairwise Anti-phase Synchronization (PAS, blue background in Figs. 9 and 10). This dynamical state corresponds to a first-order standing azimuthal mode, characterized by a nodal line that lies within the crosstalk section, thereby dividing the four thermoacoustic oscillators into two pairs [10,12,14,60]. In the case of PAS, 4 ring-coupled CTOs are divided into two groups in which two CTOs are in-phase synchronized, and

two groups are anti-phase synchronized. For example, Fig. 10(E9) shows that $\psi_{\tilde{p}',2}$ and $\psi_{\tilde{p}',3}$ remain constant with a mean value lying within a range of $|\psi| > \pi/2$, indicating anti-phase synchronization between CTO1 and CTO2 as well as CTO3. By contrast, $\psi_{\tilde{p}',4}$ remains constant with a mean value lying within a range of $|\psi_{\tilde{p}',4}| < \pi/2$, indicating in-phase synchronization between CTO1 and its adjacent oscillator (CTO4). This phase relationship is captured numerically by the model as shown in Fig. 10(S9), where $\psi_{\tilde{x}',2} > \pi/2$, $\psi_{\tilde{x}',3} > \pi/2$, and $-\pi/2 < \psi_{\tilde{x}',4} < \pi/2$. In addition to the phase relationship, we notice that 4 peaks of $\tilde{p}'$ share the same frequency with a shift from $\tilde{f} = 1$, where the natural frequency of DTO is, to $\tilde{f} = 1.17$, as shown in Fig. 9(E9). While we previously observed frequency shifts due to synchronization in the cases of $\eta_1 = 0.40$ or $\eta_2 = 0.31$, this phenomenon is more pronounced for long combustor with $\eta_3 = 0.25$. Furthermore, we observe this frequency shift not only in the case of PAS, but also in the cases of 2AS ($\tilde{f} = 1 \rightarrow 1.10$, Fig. 9(E5)) and AAS ($\tilde{f} = 1 \rightarrow 1.20$, Fig. 9(E7)). This frequency shift is compensated for using the reactive coupling in the model. For example, we see the frequency shifts from the natural frequency $\tilde{\omega} = 1$ to 1.06 in the case of 2AS (Fig. 9(S5)), to 1.09 in the case of AAS (Fig. 9(S7)), and to 1.07 in the case of PAS (Fig. 9(S9)). However, there are still some special collective dynamics observed in the experiments for $\eta_3 = 0.25$ that cannot be reproduced numerically by the model. One such phenomenon is the emergence of a weak breathing chimera (CH, Fig. 9(E1)). It emerges when four identical self-excited DTOs are ring-coupled, but only in the long combustor. This collective state involves spatiotemporal variations in the synchronization state of coupled oscillators in a network, which was first studied by Abrams et al. [62]. For more details on this weak breathing chimera, please refer to our previous studies by Guan et al. [11,28]. Although the model is unable to reproduce the complex temporal variation in the phase relationship for all three self-excited modes, it can reproduce the phase relationship of the highest frequency (i.e., 201 Hz). By applying the bandpass filter to this specific frequency, we find that CTO1 is in-phase synchronized with CTO3, while being anti-phase synchronized with CTO2 and CTO4 in Fig. 10(E1). Similarly, CVO1 is in-phase synchronized with CVO3 ($|\psi_{\tilde{x}',3}| < \pi/2$), while being anti-phase synchronized with CVO2 and CVO4 ($|\psi_{\tilde{x}',2}| > \pi/2$ and $|\psi_{\tilde{x}',4}| > \pi/2$) in Fig. 10(S1).
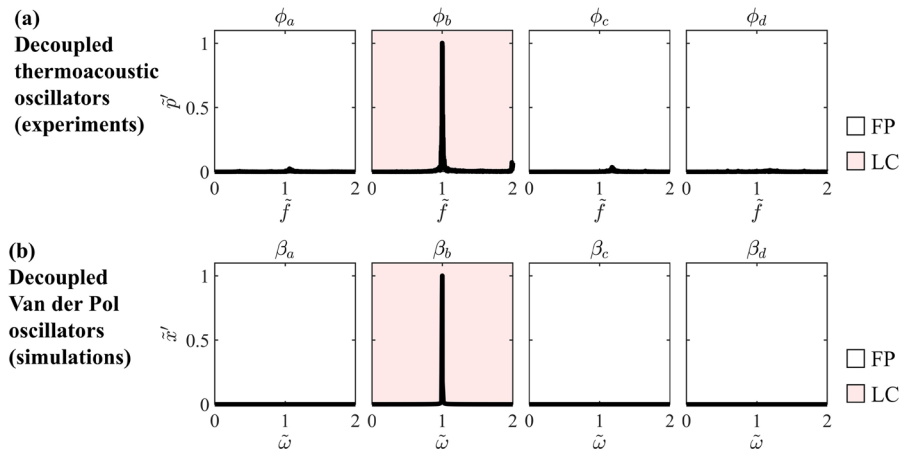
Fig. 8 The same as for Fig. 2 but when $\eta_3 = 0.25$. Each β_i ($i = a, b, c, d$) denotes a combination of λ_i and ω_i in simulations as per $(\phi_a, \phi_b, \phi_c, \phi_d)$=(0.57, 0.61, 0.65, 0.69) in experiments. $\beta_i = (\lambda_i, \omega_i)$ of each decoupled VDP oscillator is calibrated using $\tilde{p}'$ and $\tilde{f}$ of its corresponding thermoacous-tic oscillator, which gives $\beta_a = (\lambda_a, \omega_a) = (-0.03, 0.99)$, $\beta_b = (\lambda_b, \omega_b) = (0.05, 1)$, $\beta_c = (\lambda_c, \omega_c) = (-0.03, 1.01)$, $\beta_d = (\lambda_d, \omega_d) = (-0.03, 1.02)$. Legend: FP = fixed point; LC = limit cycle
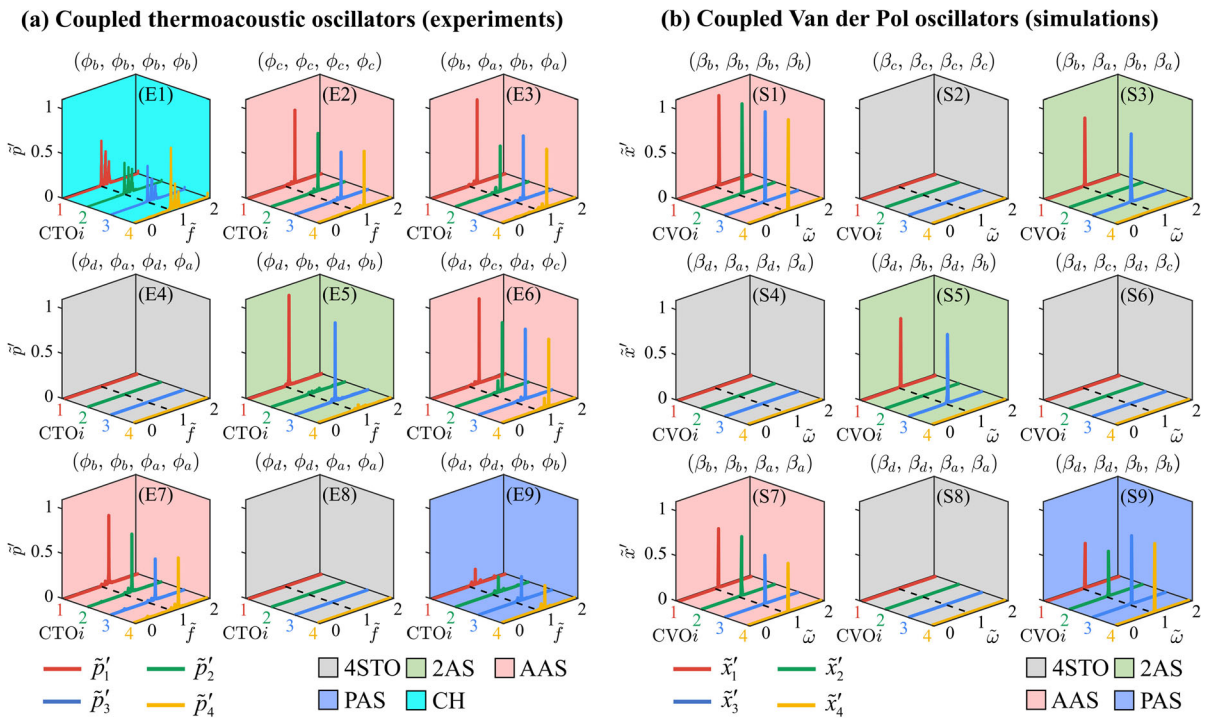
Fig. 9 The same as for Fig. 3 but when $\eta_3 = 0.25$. Coupling parameters (k_d, k_τ, k_r, τ) of the coupled VDP oscillators are calibrated using experimental results, which gives $k_d = k_\tau = 0.002$, $k_r = 0.05$, $\tau = 1.6$. Legend: 2AS = 2-can anti-phase synchro-nization; AAS = alternating anti-phase synchronization; PAS = pairwise anti-phase synchronization; 4STO = 4 steady thermoa-coustic oscillators; CH = weak chimera
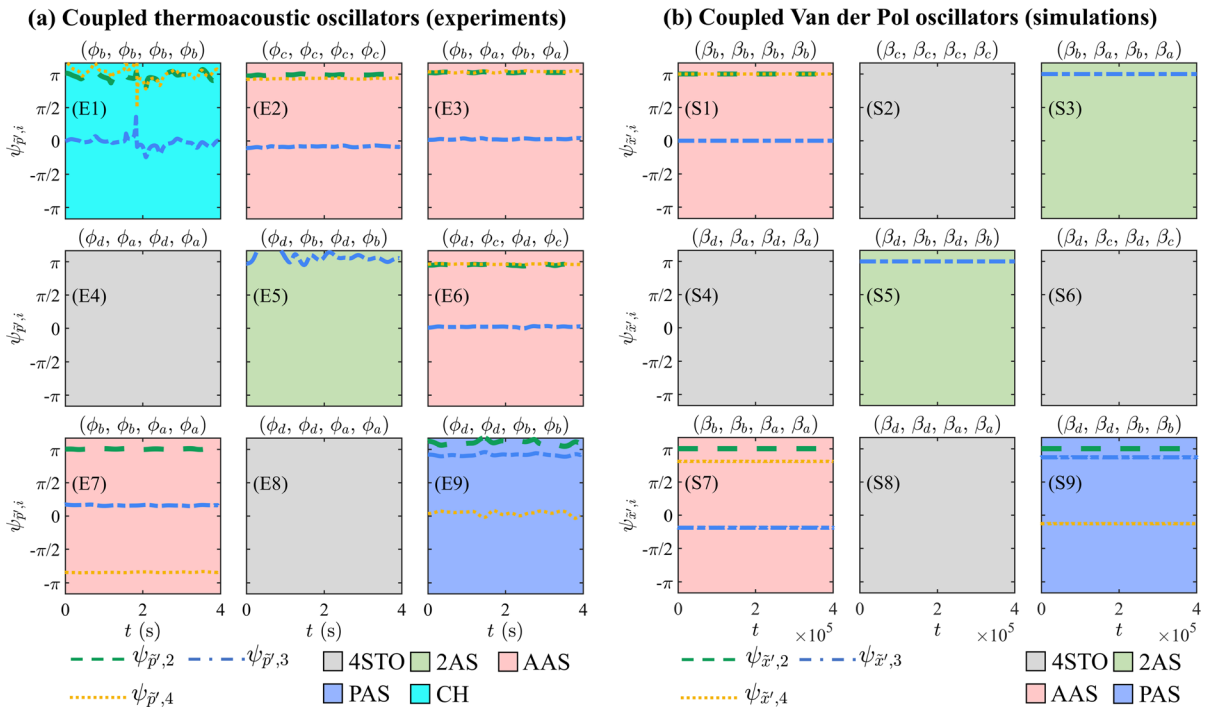
Fig. 10 The same as for Fig. 4 but when $\eta_3 = 0.25$. Legend: 2AS = 2-can anti-phase synchronization; AAS = alternating anti-phase synchronization; PAS = pairwise anti-phase synchronization; 4STO = 4 steady thermoacoustic oscillators; CH = weak chimera

Besides, the coupling-induced excitation of the thermoacoustic mode discussed in Sect. 3.1 (e.g., Fig. 9 (E2) and (E6)) is also unable to be reproduced numerically.

4 Identification of amplitude death regions

Although many collective dynamics were found in this network of four ring-coupled thermoacoustic oscillators [9,10], the global/partial amplitude death (AD), which was reported in our two-can experiments before [26,27] and holds great value for the development of passive control strategies, is absent. In this section, we use the calibrated low-order model to numerically identify the parameter region of amplitude death.

We begin by investigating the influence of coupling parameters on AD. The coupling parameters under consideration are the dissipative and time-delay coupling strengths, k_d and k_τ, along with the time delay τ. The influence of the reactive coupling strength, k_r, is excluded as it is unrelated to the occurrence of AD [52]. For the four oscillators, we set $\beta_i = \beta_d$, which is the same as the one used in Fig. 5, as the cases with

$\eta_2 = 0.31$ provide the best match to the experimental results discussed in Sect. 3.2. We expand the parametric region by varying k_d and k_τ ($k_d = k_\tau$) within the range of [0.001, 0.016] with a step size of 0.001, and τ within the range of [1, 3] with a step size of 0.1. The results are shown in Fig. 11a, where $\mu_{\tilde{x}'}$ is the mean of four normalized amplitudes of CVOs, i.e., $1/4 \sum_{i=1}^{4} \tilde{x}_i'$. We observe that AD tends to occur in the presence of stronger coupling between oscillators, indicated by larger values of k_d or k_τ, and shorter time delays, indicated by smaller values of τ. The case circled by the blue box corresponds to the case in Fig. 6(E2), which is close to the boundary of AD. Although amplitude death is absent in our experiments [9,10], our developed low-order model has enabled us to identify the parameter space where amplitude death is likely to manifest. Figure 11 suggests that a stronger coupling strength and a shorter delay time are conducive to the emergence of amplitude death. We can deduce that, for a practical can-annular combustor, a wider gap between the combustor exit and the turbine inlet, facilitating enhanced acoustic communication between adjacent cans possibly, as well as a compact arrangement of combus-
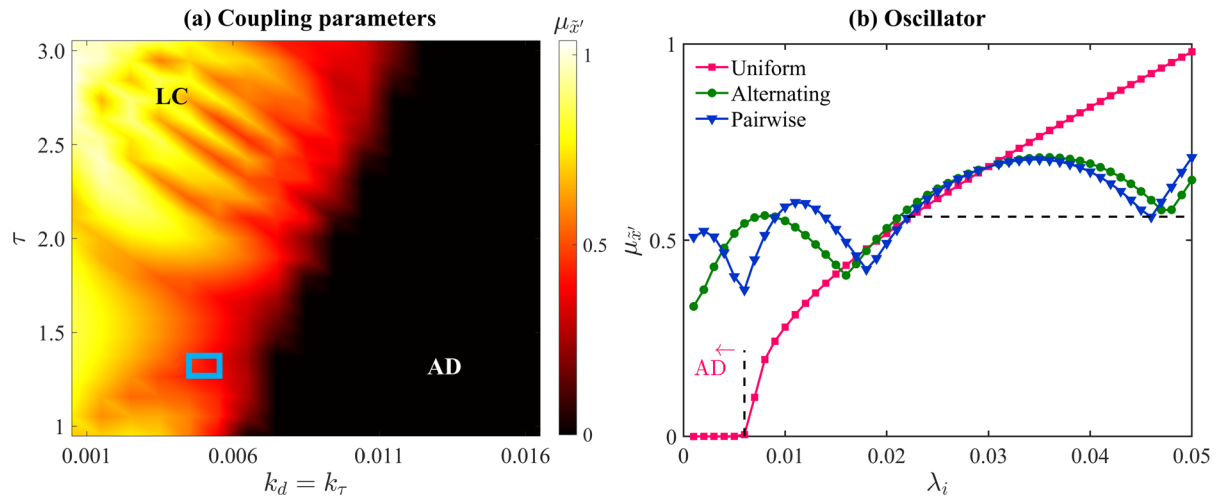
Fig. 11 Panel **a** shows the variation of the mean oscillation amplitude of coupled VDP oscillators, i.e., $\mu_{\tilde{x}'} = 1/4 \sum_{i=1}^{4} \tilde{x}'_i$, in the parameter space defined by the dissipative and time-delay coupling strength, $k_d = k_\tau$, and the time delay, τ. The case circled by the blue box corresponds to the case in Fig. 5(E2). Panel

b shows the variation of $\mu_{\tilde{x}'}$ as a function of oscillator parameters, λ_i, with three different ring-coupled patterns of coupled oscillators (uniform, alternating, and pairwise). Legend: LC = limit cycle; AD = amplitude death

tors, leading to shorter time delays in acoustic communication between adjacent cans, may promote the occurrence of AD. However, it should be noted that these dimensions are relatively less flexible to adjust compared to modifying the properties of the thermoacoustic oscillator (e.g., amplitude/frequency) and their coupling patterns (e.g., uniform/alternating/pairwise). Therefore, we explore the possibility of inducing AD or oscillation suppression through the adjustment of the properties of coupled oscillators in the model.

We still consider three coupling patterns of CVOs analogous to the combinations of equivalence ratios here. In the uniform cases, we tune λ_i in the range of [0.001, 0.05] with a stepsize of 0.001 and fix $\omega_i = 1$ for all four oscillators. In the alternating cases, we fix λ_i and ω_i of two diagonally coupled oscillators (1 and 3) to be 0.03 and 1, respectively, and tune the λ_i of the other two coupled oscillators (2 and 4) in the range of [0.001, 0.05] with a stepsize of 0.001 while fixing their ω_i to be 1. In the pairwise cases, we fix λ_i and ω_i of two adjacently coupled oscillators (1 and 2) to be 0.03 and 1, respectively, and tune the λ_i of the other two coupled oscillators (3 and 4) in the range of [0.001, 0.05] with a stepsize of 0.001 while fixing their ω_i to be 1. The coupling parameters remain identical to those used in the cases of $\eta_2 = 0.31$ ($k_d = k_\tau = 0.004$, $k_r = 0.01$,

$\tau = 1.3$). As shown in Fig. 11b, AD emerges only in the uniform cases when $\lambda_i \leqslant 0.006$. This is probably because $\tilde{x}'$ is relatively small. Beyond this critical λ_i, $\mu_{\tilde{x}'}$ monotonically increases as λ_i increases. This could be because $\tilde{x}'$ grows as λ_i increases without the emergence of any oscillation suppression mechanism. By contrast, for the alternating and pairwise cases, the local minimum of $\mu_{\tilde{x}'}$ intermittently appears (at different λ_i for two different combinations). Leveraging these local minima of $\mu_{\tilde{x}'}$, we can achieve a substantially large reduction in $\mu_{\tilde{x}'}$ by slightly adding asymmetry to the model. For example, at the right end of the horizontal dashed line, the pairwise cases exhibit a local minimum of $\mu_{\tilde{x}'}$ when $\lambda_1 = \lambda_2 = 0.03$ and $\lambda_3 = \lambda_4 = 0.046$. On the other hand, at the left end of the horizontal dashed line, a uniform case has $\lambda_i = 0.022$. As $\tilde{x}'$ monotonically increases with λ, the decoupled oscillators in the pairwise case naturally possess higher $\tilde{x}'$ compared to the decoupled oscillators in the uniform case. However, after being ring-coupled with a pairwise pattern, they roughly exhibit the same value of $\mu_{\tilde{x}'}$ as those being ring-coupled with a uniform pattern. This implies that the asymmetric arrangement of coupled oscillators can potentially lead to oscillation suppression, which could favor the development of passive control strategies.

5 Conclusions

In this study, we investigate the low-order modeling of collective dynamics in a can-annular combustor consisting of four ring-coupled turbulent thermoacoustic oscillators. The model contains four VDP oscillators ring-coupled through dissipative, time-delay, and reactive coupling terms. By meticulously calibrating the parameters of the model using experimental data, we show that this model, though in a simple form, can successfully reproduce many collective dynamics observed in experiments under different combinations of equivalence ratio and combustor lengths, such as 2-can anti-phase synchronization, alternating anti-phase synchronization, pairwise anti-phase synchronization, spinning azimuthal mode, and 4 steady thermoacoustic oscillators. The phase relationship of most coupled cases can also be modeled both qualitatively and quantitatively. Furthermore, with the introduction of the reactive coupling term, the model is now more adaptive to reproduce the frequency shift in cases showing strong energy transformation. However, certain complex collective dynamics remain beyond the model's reach. These include (i) the excitation of a coupling-induced unstable thermoacoustic mode when four steady decoupled thermoacoustic oscillators (DTOs) are ring-coupled, e.g., Fig. 3(E1); (ii) the mode localization in the short combustor when four DTOs are ring-coupled under the pairwise ϕ combination with two of them being steady and the remaining two being unsteady, e.g., Fig. 3(E8); (iii) a weak anti-phase chimera in the short combustor when four DTOs are ring-coupled under the alternating ϕ combination with two of them being steady and the remaining two being unsteady, e.g., Fig. 3(E3); (iv) superposition of anti-phase synchronization in the medium combustor when four DTOs ring-coupled under the pairwise ϕ combination with two of them being steady and the remaining two being unsteady, e.g., Fig. 6(E7); and (v) a weak breathing chimera in the long combustor when four identical self-excited DTOs are ring-coupled, e.g., Fig. 9(E1). Despite these limitations, the model provides a satisfactory reproduction of a wide range of collective dynamics, given the fact that the model has such a simple structure and the experimental results were found in such a complex turbulent combustion system with unavoidable uncertainties (e.g., manufacturing, operating conditions). This study offers some valuable insights: (1) Combinations of self-excited/stable oscillators greatly affect collective dynamics, which could be interpreted and modeled within the synchronization framework; (2) The suppression of self-excited oscillations in a ring-coupled network is closely associated with the coupling conditions and the combination of self-excited oscillators. Low-order modeling opens up possibilities for identifying the optimal parameter regimes or oscillator combinations leading to weakened oscillations; (3) The low-order model is able to be extended to a system with multiple oscillators, which could potentially serves as a basis for modeling the collective dynamics observed in more complicated multi-combustor systems.

Data availability The data that support the findings of this study are available from the corresponding author upon reasonable request.

Declaration

Conflict of interest The authors declare that they have no conflict of interest.

Appendix A: Influence of experimental uncertainties on the modeling

Due to uncertainties in manufacturing and operating conditions (such as equivalence ratio ϕ, inlet temperature T_{inlet}, and bulk velocity $\bar{u}$) in experiments, noticeable differences in the properties of thermoacoustic instability (such as pressure amplitude and natural frequency) can be observed between two nominally identical combustors. These subtle differences in DTOs have significant influences on the properties of CTOs, which pose challenges in calibrating the model parameters using experimental data. We find that the pressure ratio between two nominally identical thermoacoustic oscillators can be better reproduced by specifically tuning the parameters for a particular VDP oscillator. For example, as shown in Fig. 12(E1), there is a small amplitude difference between $\tilde{p}'_1$ and $\tilde{p}'_3$, although they share the same value of ϕ. As shown in Fig. 12(S1), by slightly tuning β_d to β_d^* for the third VDP oscillator, we are able to more accurately reproduce the pressure ratio observed in experiments. This approach holds true for combustors of different lengths as well (Fig. 12(S2)→(E2), (S3)→(E3)). Although this
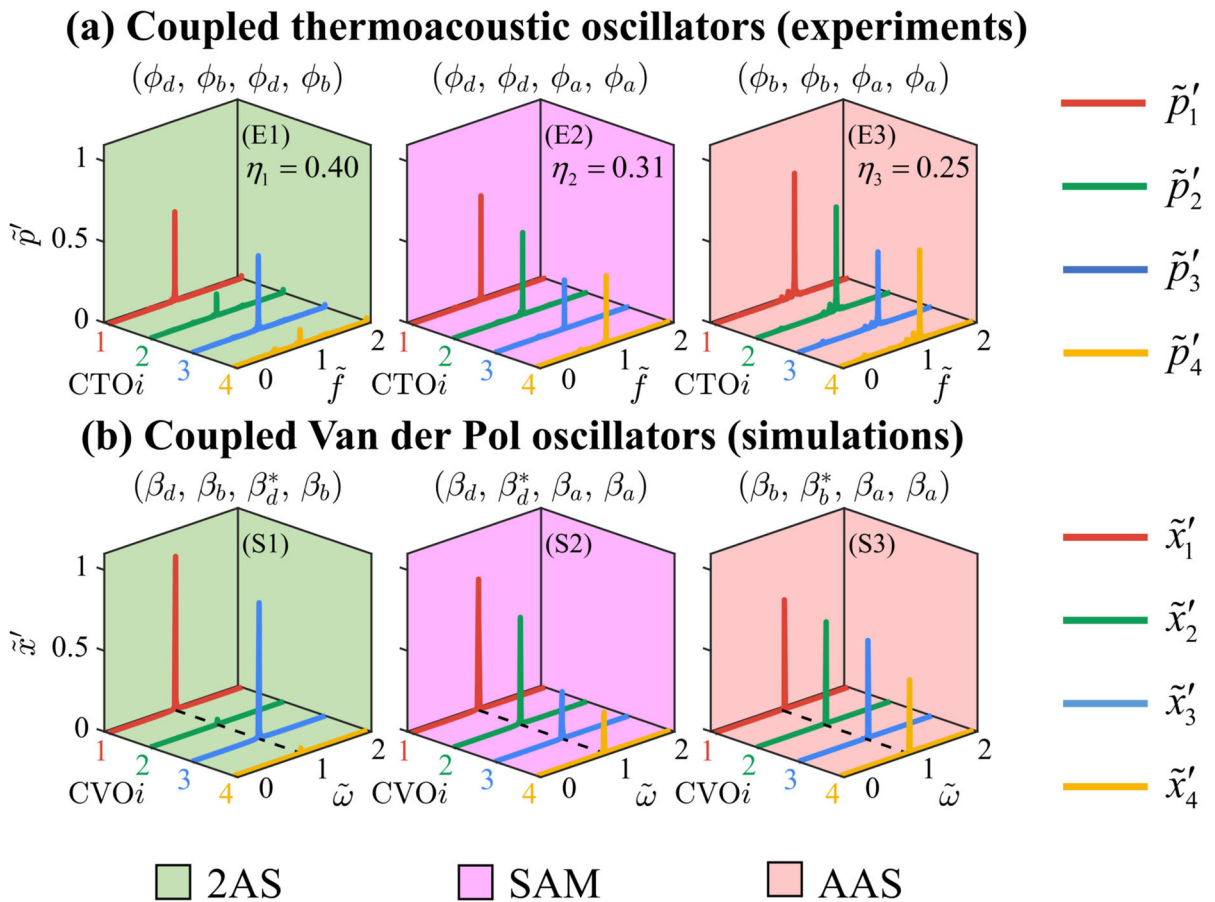

Fig. 12 Spectral comparison between (top) coupled thermoacoustic oscillators (experiments) and (bottom) coupled VDP oscillators (simulations). Each β_i ($i = a, b, c, d$) denotes a combination of λ_i and ω_i in simulations, corresponding to $(\phi_a, \phi_b, \phi_c, \phi_d)$=(0.57, 0.61, 0.65, 0.69) in experiments. The symbol * indicates the compensation applied to the nominally identical VDP oscillators by slightly adjusting λ. The parameters of the model of three cases are: $(\lambda_d, \lambda_b, \lambda_d^*, \lambda_b)$ = $(0.05, -0.01, 0.042, -0.01)$, $(\lambda_c, \lambda_c^*, \lambda_a, \lambda_a)$ = $(0.048, 0.025, -0.02, -0.02)$, $(\lambda_b, \lambda_b^*, \lambda_a, \lambda_a)$ = $(0.05, 0.035, -0.03, -0.03)$. ω_i and coupling parameters (k_d, k_τ, k_r, and τ) are the same as the corresponding case shown in Fig. 3(E6), Fig. 6(E8), Fig. 9(E7). Legend: 2AS = 2-can anti-phase synchronization; SAM = spinning azimuthal mode; AAS = alternating anti-phase synchronization
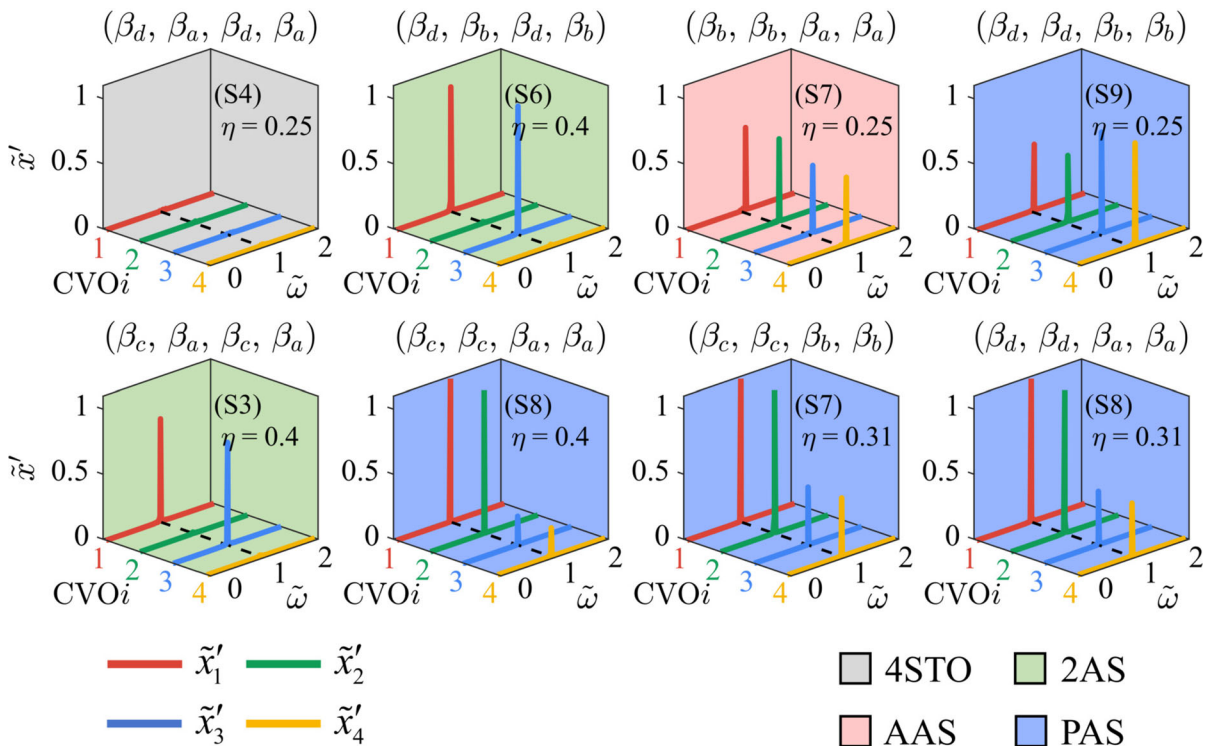
Fig. 13 FFT spectra of typical collective dynamics with noise intensity of $\sigma = 0.04$. The dashed line in the subfigure denotes the position of $\tilde{f} = 1$ and $\tilde{\omega} = 1$, respectively. Legend: 4STO = 4 steady thermoacoustic oscillators; 2AS = 2-can anti-phase synchronization; AAS = alternating anti-phase synchronization; PAS = pairwise anti-phase synchronization

fine-tuning of model parameters for specific oscillators yields more accurate spectra, it weakens the simplicity of our modeling approach and diminishes the model's ability to reproduce complex collective dynamics. We therefore do not incorporate such compensation in the calibration process.

Appendix B: Influence of noise term on the modeling

The influence of turbulent combustion noise on system dynamics is important in modeling, particularly when modeling statistical properties of thermoacoustic oscillators [63–66]. However, the addition of a noise source term in our model did not enhance the modeling results. This could be attributed to the thermoacoustic oscillators (both stable and self-excited) selected for this study being sufficiently distant from the bifurcation point, making turbulent combustion noise have a reduced impact on the properties of the thermoacoustic oscillator. Additionally, this study primarily focuses on modeling coupling-induced dynamics arising from thermoacoustic modal interactions rather than the

statistical properties of thermoacoustic modes, placing less emphasis on the influence of turbulent combustion noise. The noise term is often not included under such a scenario in previous studies [39,41,67].

Our VDP model, Eq. (1), becomes Eq. (B1) after including a noise source term:

$$\ddot{x}_i - \left(\lambda_i - x_i^2\right)\dot{x}_i + \omega_i^2 x_i = \underbrace{k_d\left(\dot{x}_{i+1} + \dot{x}_{i-1} - 2\dot{x}_i\right)}_{Dissipative\ coupling}$$

$$+ \underbrace{k_\tau[\dot{x}_{i+1}(t-\tau) + \dot{x}_{i-1}(t-\tau) - 2\dot{x}_i]}_{Time-delay\ coupling}$$

$$+ \underbrace{k_r\left(x_{i+1} + x_{i-1} - 2x_i\right)}_{Reactive\ coupling} + \underbrace{\sigma\epsilon(t)}_{Noise} \qquad (B1)$$

where σ is noise intensity, $\epsilon(t)$ is a white Gaussian noise term, and all other parameters remain identical to Eq. (1). We use the pressure data of stable decoupled thermoacoustic oscillators (e.g., ϕ_a case in Fig. 2/5/8) to evaluate the combustion noise intensity and acquired a dimensionless noise intensity $\sigma = 0.04$. Next, we present FFT spectra and phase relationship of typical collective dynamics reproduced with noise in Fig. 13
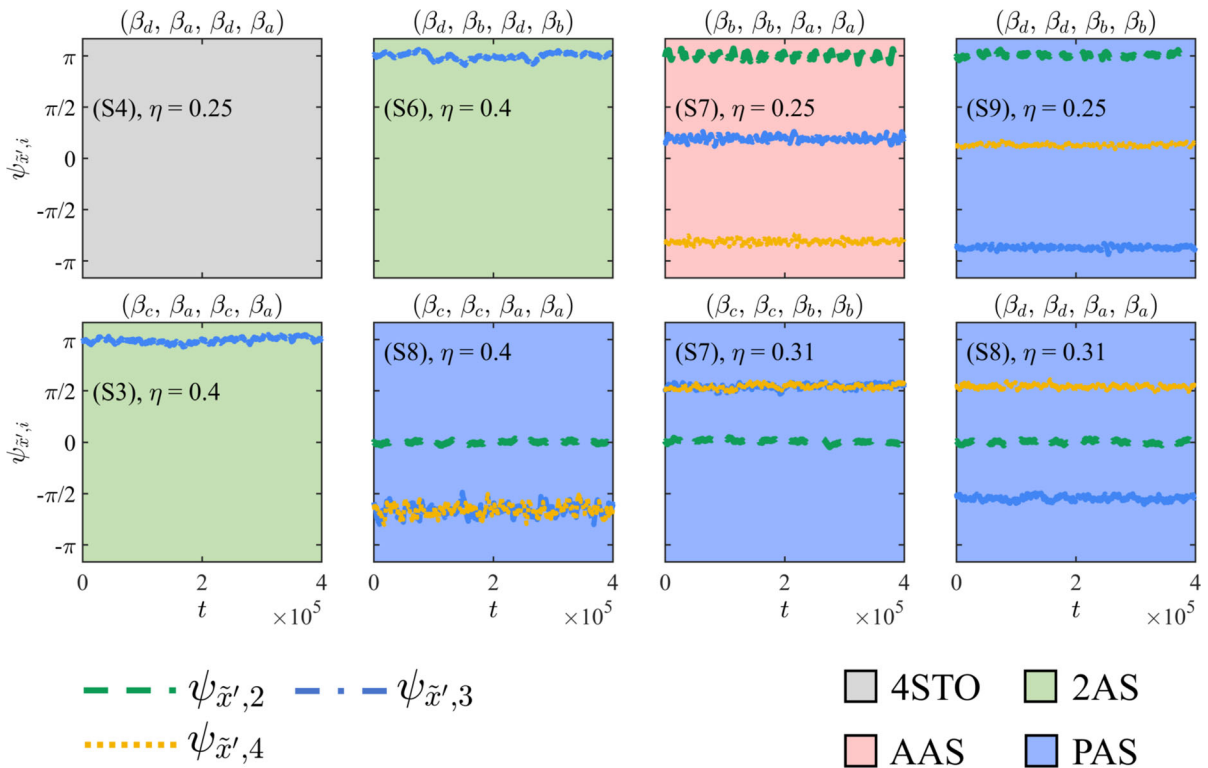
Fig. 14 Phase relationship of typical collective dynamics with noise intensity of $\sigma = 0.04$. The presentation of $\psi_{\tilde{p}',i}$ and $\psi_{\tilde{x}',i}$ follows the same format as illustrated in Fig. 4. The legend remains consistent with the FFT spectra in Fig. 13

and Fig. 14, respectively. The results show that including the noise term does not enhance the modeling results. Most of collective dynamics can still be reproduced well although noticeable shifts and undulations emerge in phase relationships. On the contrary, some collective dynamics which were originally successfully reproduced without noise term cannot be reproduced now (e.g., Fig. 13(S8)). Therefore, we prefer not include the noise term in our current model.

Appendix C: Influence of parametric noise on the modeling

Parametric noise can possibly affect the modeling results as shown in previous studies [40,68,69]. Here we incorporate parametric noise into our model by introducing noise in six parameters, including the oscillator parameters λ and ω and the coupling parameters k_d, k_τ, k_r, and τ. The corresponding parameters with the noise term can be expressed as follows:

$$X_n = X_0[1 + \sigma_p \epsilon(t)]$$
$$(X = \lambda \,/\, \omega \,/\, k_d \,/\, k_\tau \,/\, k_r \,/\, \tau) \tag{C2}$$

where X_n and X_0 represent the parameters with and without noise, respectively, σ_p is the noise intensity, and $\epsilon(t)$ is white Gaussian noise term. We use $\sigma_p = 1\%$ following previous studies [40,68,69]. Here we examine the influence of parametric noise on some typical collective dynamics discussed above. For each collective dynamics, parametric noise is added to only one single parameter. As shown in Fig. 15, each panel is divided into seven shorter subfigures, which correspond to phase dynamics of cases subjected to different parametric noise. From left to right, we have parametric noise free (O), oscillator parameters (λ and ω) and coupling parameters (k_d, k_τ, k_r, and τ). The results show that most of collective dynamics are merely influenced by the parametric noise when $\sigma_p = 0.01$, regardless of parameters. Critical collective dynamics, including 4STO, 2AS, AAS, PAS, and SAM, can still be numerically reproduced well. For some specific cases ((S8), $\eta = 0.4$ and (S7), $\eta = 0.31$), collective dynamics and phase relationship changed noticeably.
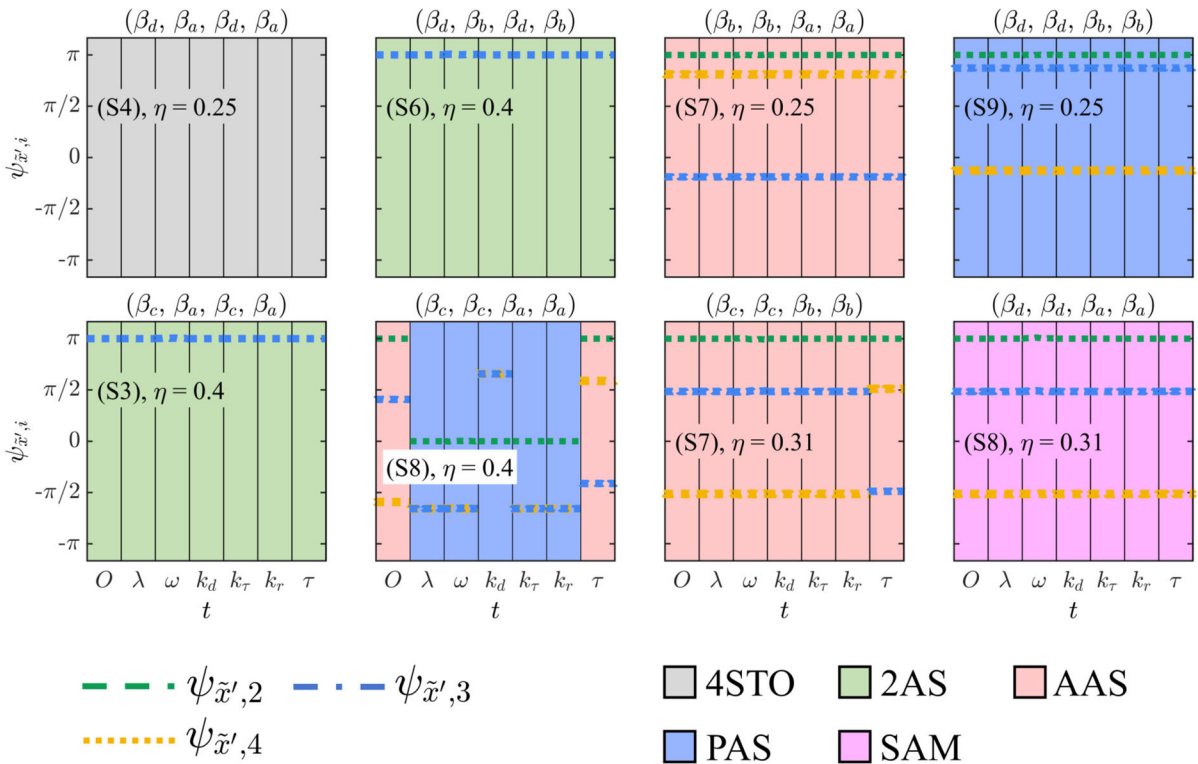
Fig. 15 Phase relationship of typical collective dynamics with parametric noise amplitude $\sigma_p = 0.01$. The presentation of $\psi_{\tilde{p}',i}$ and $\psi_{\tilde{x}',i}$ follows the same format as illustrated in Fig. 4. The abbreviation "O" represent the original noise-free case. Legend:

4STO = 4 steady thermoacoustic oscillators; 2AS = 2-can anti-phase synchronization; AAS = alternating anti-phase synchronization; PAS = pairwise anti-phase synchronization; SAM = spinning azimuthal mode

References

1. Candel, S.: Combustion dynamics and control: progress and challenges. Proc. Combust. Inst. **29**(1), 1–28 (2002)
2. Lieuwen, T., Yang, V.: Combustion Instabilities in Gas Turbine Engines: Operational Experience, Fundamental Mechanisms, and Modeling. American Institute of Aeronautics and Astronautics, Reston (2005)
3. Rayleigh, L.: The explanation of certain acoustical phenomena. Roy. Inst. Proc. **8**, 536–542 (1878)
4. Huang, Y., Yang, V.: Dynamics and stability of lean-premixed swirl-stabilized combustion. Prog. Energy Combust. **35**(4), 293–364 (2009)
5. Poinsot, T.: Prediction and control of combustion instabilities in real engines. Proc. Combust. Inst. **36**(1), 1–28 (2017)
6. O'Connor, J.: Understanding the role of flow dynamics in thermoacoustic combustion instability. Proc. Combust. Inst. **39**, 4583–4610 (2022)
7. Luque, S., Kanjirakkad, V., Aslanidou, I., Lubbock, R., Rosic, B., Uchida, S.: A new experimental facility to investigate combustor-turbine interactions in gas turbines with multiple can combustors. J. Eng. Gas Turbines Power **137**(5), 051503 (2015)
8. Farisco, F., Panek, L., Kok, J.: Thermo-acoustic cross-talk between cans in a can-annular combustor. Int. J. Spray Combust. Dyn. **9**(4), 452–469 (2017)
9. Moon, K., Jegal, H., Yoon, C., Kim, K.: Cross-talk-interaction-induced combustion instabilities in a can-annular lean-premixed combustor configuration. Combust. Flame **220**, 178–188 (2020)
10. Moon, K., Yoon, C., Kim, K.: Influence of rotational asymmetry on thermoacoustic instabilities in a can-annular lean-premixed combustor. Combust. Flame **223**, 295–306 (2021)
11. Guan, Y., Li, L., Jegal, H., Kim, K.: Effect of flame response asymmetries on the modal patterns and collective states of a can-annular lean-premixed combustion system. Proc. Combust. Inst. **39**(4), 4731–4739 (2023)
12. Moon, K., Choi, Y., Kim, K.: Experimental investigation of lean-premixed hydrogen combustion instabilities in a can-annular combustion system. Combust. Flame **235**, 111697 (2022)
13. Buschmann, P., Worth, N., Moeck, J.: Thermoacoustic oscillations in a can-annular model combustor with asymmetries in the can-to-can coupling. Proc. Combust. Inst. **39**, 5707–5715 (2022)

14. Ghirardo, G., Di Giovine, C., Moeck, J., Bothien, M.: Thermoacoustics of can-annular combustors. J. Eng. Gas Turbines Power **141**(1), 011007 (2019)

15. Ghirardo, G., Moeck, J., Bothien, M.: Effect of noise and nonlinearities on thermoacoustics of can-annular combustors. J. Eng. Gas Turbines Power **142**(4), 041005 (2020)

16. von Saldern, J., Orchini, A., Moeck, J.: Analysis of thermoacoustic modes in can-annular combustors using effective Bloch-type boundary conditions. J. Eng. Gas Turbines Power **143**(7), 071019 (2021)

17. Humbert, S., Orchini, A.: Acoustics of can-annular combustors: experimental characterisation and modelling of a lab-scale multi-can setup with adjustable geometry. J. Sound Vib. **564**, 117864 (2023)

18. von Saldern, J., Moeck, J., Orchini, A.: Nonlinear interaction between clustered unstable thermoacoustic modes in can-annular combustors. Proc. Combust. Inst. **38**(4), 6145–6153 (2021)

19. Haeringer, M., Polifke, W.: Time-domain Bloch boundary conditions for efficient simulation of thermoacoustic limit cycles in (can-) annular combustors. J. Eng. Gas Turbines Power **141**(12), 121005 (2019)

20. Haeringer, M., Polifke, W.: Hybrid CFD/low-order modeling of thermoacoustic limit cycle oscillations in can-annular configurations. Int. J. Spray Combust. Dyn. **14**(1–2), 143–152 (2022)

21. Fournier, G., Schaefer, F., Haeringer, M., Silva, C., Polifke, W.: Interplay of clusters of acoustic and intrinsic thermoacoustic modes in can-annular combustors. J. Eng. Gas Turbines Power **144**(12), 121015 (2022)

22. Sujith, R., Unni, V.: Complex system approach to investigate and mitigate thermoacoustic instability in turbulent combustors. Phys. Fluids **32**(6), 061401 (2020)

23. Sujith, R., Unni, V.: Dynamical systems and complex systems theory to study unsteady combustion. Proc. Combust. Inst. **38**(3), 3445–3462 (2021)

24. Hyodo, H., Iwasaki, M., Biwa, T.: Suppression of Rijke tube oscillations by delay coupling. J. Appl. Phys. **128**(9), 094902 (2020)

25. Saxena, G., Prasad, A., Ramaswamy, R.: amplitude death: the emergence of stationarity in coupled nonlinear systems. Phys. Rep. **521**(5), 205–228 (2012)

26. Jegal, H., Moon, K., Gu, J., Li, L., Kim, K.: Mutual synchronization of two lean-premixed gas turbine combustors: phase locking and amplitude death. Combust. Flame **206**, 424–437 (2019)

27. Moon, K., Guan, Y., Li, L., Kim, K.: Mutual synchronization of two flame-driven thermoacoustic oscillators: dissipative and time-delayed coupling effects. Chaos **30**(2), 023110 (2020)

28. Guan, Y., Moon, K., Kim, K., Li, L.: Synchronization and chimeras in a network of four ring-coupled thermoacoustic oscillators. J. Fluid Mech. **938**, 5 (2022)

29. Biwa, T., Tozuka, S., Yazaki, T.: Amplitude death in coupled thermoacoustic oscillators. Phys. Rev. Appl. **3**(3), 034006 (2015)

30. Hyodo, H., Biwa, T.: Stabilization of thermoacoustic oscillators by delay coupling. Phys. Rev. E **98**(5), 052223 (2018)

31. Dange, S., Manoj, K., Banerjee, S., Pawar, S., Mondal, S., Sujith, R.: Oscillation quenching and phase-flip bifurcation in coupled thermoacoustic systems. Chaos **29**(9), 093135 (2019)

32. Chen, G., Li, Z., Tang, L., Yu, Z.: Mutual synchronization of self-excited acoustic oscillations in coupled thermoacoustic oscillators. J. Phys. D Appl. Phys. **54**(48), 485504 (2021)

33. Fournier, G., Meindl, M., Silva, C., Ghirardo, G., Bothien, M., Polifke, W.: Low-order modeling of can-annular combustors. J. Eng. Gas Turbines Power **143**(12), 121004 (2021)

34. Yoon, M.: Thermoacoustics and combustion instability analysis for multi-burner combustors. J. Sound Vib. **492**, 115774 (2021)

35. Yoon, M.: Thermoacoustics of multi-burner combustors with plenum and chamber cross-talk. J. Sound Vib. **520**, 116623 (2022)

36. Orchini, A., Pedergnana, T., Buschmann, P., Moeck, J., Noiray, N.: Reduced-order modelling of thermoacoustic instabilities in can-annular combustors. J. Sound Vib. **526**, 116808 (2022)

37. Bonciolini, G., Noiray, N.: Bifurcation dodge: avoidance of a thermoacoustic instability under transient operation. Nonlinear Dyn. **96**, 703–716 (2019)

38. Bonciolini, G., Noiray, N.: Synchronization of thermoacoustic modes in sequential combustors. J. Eng. Gas Turbines Power **141**(3), 03101 (2019)

39. Moeck, J., Durox, D., Schuller, T., Candel, S.: Nonlinear thermoacoustic mode synchronization in annular combustors. Proc. Combust. Inst. **37**(4), 5343–5350 (2019)

40. Bonciolini, G., Faure-Beaulieu, A., Bourquard, C., Noiray, N.: Low order modelling of thermoacoustic instabilities and intermittency: flame response delay and nonlinearity. Combust. Flame **226**, 396–411 (2021)

41. Guan, Y., Moon, K., Kim, K., Li, L.: Low-order modeling of the mutual synchronization between two turbulent thermoacoustic oscillators. Phys. Rev. E **104**(2), 024216 (2021)

42. Weng, Y., Unni, V.R., Sujith, R.I., Saha, A.: Synchronization framework for modeling transition to thermoacoustic instability in laminar combustors. Nonlinear Dyn. **100**, 3295–3306 (2020)

43. Weng, Y., Unni, V., Sujith, R., Saha, A.: Synchronization based model for turbulent thermoacoustic systems. Nonlinear Dyn. **111**(13), 12113–12126 (2023)

44. Pedergnana, T., Noiray, N.: Steady-state statistics, emergent patterns and intermittent energy transfer in a ring of oscillators. Nonlinear Dyn. **108**(2), 1133–1163 (2022)

45. Wildemans, R., Kornilov, V., Lopez, T.: Parameter estimation of two coupled oscillator model for pure intrinsic thermo-acoustic instability. Nonlinear Dyn. **111**, 1–19 (2023)

46. Guan, Y., Gupta, V., Kashinath, K., Li, L.: Open-loop control of periodic thermoacoustic oscillations: experiments and low-order modelling in a synchronization framework. Proc. Combust. Inst. **37**(4), 5315–5323 (2019)

47. Ramanan, V., Ramankutty, A., Sreedeep, S., Chakravarthy, S.: Dynamical states of thermo-acoustic system with respect to frequency-phase relationship based on probabilistic oscillator model. Nonlinear Dyn. **110**(2), 1633–1649 (2022)

48. Guan, Y., Gupta, V., Wan, M., Li, L.: Forced synchronization of quasiperiodic oscillations in a thermoacoustic system. J. Fluid Mech. **879**, 390–421 (2019)

49. Guan, Y., Yin, B., Yang, Z., Li, L.: Forced synchronization of self-excited chaotic thermoacoustic oscillations. J. Fluid Mech. **982**, A9 (2024)

50. Thomas, N., Mondalirshendu, S., Pawarmadhan, S., Sujith, R.: Effect of noise amplification during the transition to amplitude death in coupled thermoacoustic oscillators. Chaos **28**(9), 093116 (2018)

51. Balanov, A., Janson, N., Postnov, D., Sosnovtseva, O.: Synchronization: From Simple to Complex. Springer, Heidelberg (2009)

52. Pikovsky, A., Rosenblum, M., Kurths, J.: Synchronization: A Universal Concept in Nonlinear Sciences. Cambridge Nonlinear Science Series, Cambridge University Press, United Kingdom (2001)

53. Landa, P.: Nonlinear Oscillations and Waves in Dynamical Systems. Mathematics and Its Applications. Springer, Dordrecht (2013)

54. Wang, J., Li, X.: Reactive coupling effects on amplitude death of coupled limit-cycle systems. Chin. Phys. Lett. **26**(3), 030505 (2009)

55. Vakakis, A., Manevitch, L., Mikhlin, Y., Pilipchuk, V., Zevin, A.: Normal Modes and Localization in Nonlinear Systems. Springer, Dordrecht (2001)

56. Ashwin, P., Burylko, O.: Weak chimeras in minimal networks of coupled phase oscillators. Chaos **25**(1), 013106 (2015)

57. Suda, Y., Okuda, K.: Persistent chimera states in nonlocally coupled phase oscillators. Phys. Rev. E **92**(6), 060901 (2015)

58. Maistrenko, Y., Brezetsky, S., Jaros, P., Levchenko, R., Kapitaniak, T.: Smallest chimera states. Phys. Rev. E **95**(1), 010203 (2017)

59. Manoj, K., Pawar, S., Dange, S., Mondal, S., Sujith, R., Surovyatkina, E., Kurths, J.: Synchronization route to weak chimera in four candle-flame oscillators. Phys. Rev. E **100**(6), 062204 (2019)

60. Kaufmann, P., Krebs, W., Valdes, R., Wever, U.: 3D thermoacoustic properties of single can and multi can combustor configurations. In: Turbo Expo: Power for Land, Sea, and Air, vol. 43130, pp. 527–538 (2008)

61. Buschmann, P., Worth, N., Moeck, J.: Thermoacoustic oscillations in a can-annular model combustor with asymmetries in the can-to-can coupling. Proc. Combust. Inst. **39**(4), 5707–5715 (2023)

62. Abrams, D., Mirollo, R., Strogatz, S., Wiley, D.: Solvable model for chimera states of coupled oscillators. Phys. Rev. Lett. **101**(8), 084103 (2008)

63. Clavin, P., Kim, J., Williams, F.: Turbulence-induced noise effects on high-frequency combustion instabilities. Combust. Sci. Technol. **96**(1–3), 61–84 (1994)

64. Lieuwen, T.: Statistical characteristics of pressure oscillations in a premixed combustor. J. Sound Vib. **260**(1), 3–17 (2003)

65. Noiray, N., Schuermans, B.: Deterministic quantities characterizing noise driven Hopf bifurcations in gas turbine combustors. Int. J. Non Linear Mech. **50**, 152–163 (2013)

66. Ghirardo, G., Boudy, F., Bothien, M.: Amplitude statistics prediction in thermoacoustics. J. Fluid Mech. **844**, 216–246 (2018)

67. Noiray, N., Bothien, M., Schuermans, B.: Investigation of azimuthal staging concepts in annular gas turbines. Combust. Theor. Model. **15**(5), 585–606 (2011)

68. Daw, C., Kennel, M., Finney, C., Connolly, F.: Observing and modeling nonlinear dynamics in an internal combustion engine. Phys. Rev. E **57**(3), 2811 (1998)

69. Burnley, V., Culick, F.: Influence of random excitations on acoustic instabilities in combustion chambers. AIAA J. **38**(8), 1403–1410 (2000)